



Investigating the temporal domain of massive ionized jets – I. A pilot study

S. J. D. Purser,^{1★} S. L. Lumsden,^{1★} M. G. Hoare^{1★} and N. Cunningham²

¹*School of Physics and Astronomy, University of Leeds, Leeds LS2 9JT, UK*

²*National Radio Astronomy Observatory, PO Box 2, Green Bank, WV 24944, USA*

Accepted 2017 November 24. Received 2017 November 22; in original form 2017 October 20

ABSTRACT

We present sensitive ($\sigma < 10 \mu\text{Jy beam}^{-1}$), radio continuum observations using the Australian Telescope Compact Array at frequencies of 6 and 9 GHz towards four massive young stellar objects (MYSOs). From a previous, less sensitive work, these objects are known to harbour ionized jets associated with radio lobes, which result from shock processes. In comparison with that work, further emission components are detected towards each MYSO. These include extended, direct, thermal emission from the ionized jet’s stream, new radio lobes indicative of shocks close ($< 10^5$ au) to the MYSO, three radio Herbig–Haro objects separated by up to 3.8 pc from the jet’s launching site, and an IR-dark source coincident with CH₃OH maser emission. No significant, integrated flux variability is detected towards any jets or shocked lobes, and only one proper motion is observed ($1806 \pm 596 \text{ km s}^{-1}$ parallel to the jet axis of G310.1420+00.7583A). Evidence for precession is detected in all four MYSOs with precession periods and angles within the ranges 66–15 480 yr and 6° – 36° , respectively. Should precession be the result of the influence from a binary companion, we infer orbital radii of 30–1800 au.

Key words: stars: formation – stars: jets – stars: massive – stars: protostars – radio continuum: general.

1 INTRODUCTION

Considering the importance of massive ($> 8 M_\odot$) stars for astrophysics in general, little is known for certain about the processes involved in their formation. The low-mass formation paradigm, in contrast, is relatively well understood (Shu, Adams & Lizano 1987). Fundamentally, inside-out collapse of a core results in the formation of a central protostar that, due to angular momentum considerations, forms a flattened disc of infalling material. Inward motion in the disc results in accretion of this material on to the forming star, with a typical rate [in the low-mass case of a $1 M_\odot$ accreting young stellar object (YSO)] of $\sim 10^{-7} M_\odot \text{ yr}^{-1}$ (Gullbring et al. 1998). Typical rates in high-mass stars, however, need to be much higher $\sim 10^{-4} M_\odot \text{ yr}^{-1}$ to accommodate for short pre-main-sequence phases ($\sim 10^5$ yr; Mottram et al. 2011). Thus, debate over how closely the accretion process mimics that of the low-mass case still ensues.

One ubiquitous feature of massive star formation is the massive molecular outflows (Beuther et al. 2002), which are detected in association with their powering massive young stellar objects (MYSOs). These outflows are thought to be mechanically coupled to jets of material, ejected perpendicular to the disc during accretion, which seems to be a common phenomenon in both low-mass (Anlada 1996) and high-mass protostars (incidence rates of ~ 65 per cent; Purser et al. 2016, from now on referred to as

Paper I). Furthermore, the ejection of jets is thought to be linked to inflow processes, with fixed accretion-to-ejection ratios for some models of jet launching/collimation (see section 2.1 in the review by Frank et al. 2014, and references therein). Therefore, the exact nature and morphology of the jets themselves can indirectly inform us on the accretion process.

From previous observations of ionized jets, their general, radio morphology seems to take the form of an elongated component with a thermal, spectral index centred on the MYSO. Theoretical studies indicate that the value for the spectral index can range from -0.1 to 1.4 (Reynolds 1986), with observational studies seemingly averaging a spectral index of ~ 0.6 (with ranges from 0.2 to 0.9 in the cases of HH 80-81 and G345.4938+01.4677, respectively; Marti, Rodríguez & Reipurth 1993; Guzmán, Garay & Brooks 2010). In ~ 50 per cent of cases, this is associated with separate lobes of emission (Paper I), which are presumably a result of the jet ionizing and shocking the ambient material of the envelope/clump, or internal shocks within the jet as a result of variability in ejection velocity (such as in the low-mass case of HH 211; Moraghan et al. 2016). These lobes tend to be spatially distinct and separate in the majority of cases (average separations of $\sim 10^4$ au; Paper I), with little radio emission seen in between thermal and non-thermal components, e.g. IRAS 16547–4247 (Rodríguez et al. 2005) and IRAS 16562–3959 (Guzmán et al. 2010). This suggests one of two possibilities, that the ejection of material is highly variable/episodic (possibly a result of fragmentation in the accretion disc; Meyer et al. 2017), or that a constant, collimated outflow of material only sporadically impinges upon the surrounding matter to form shocks.

* E-mail: purser@cp.dias.ie (SJD); s.l.lumsden@leeds.ac.uk (SLL); m.g.hoare@leeds.ac.uk (MGH)

In the cases where multiple lobes are seen, it is common to find a positional offset for the lobe from the overall position angle of the jet, suggesting that the outflow axis evolves over time. Precession of collimated outflows is predicted in the simulations of Sheikhezami & Fendt (2015) who performed 3D magnetohydrodynamic simulations of a disc–jet system influenced by the gravitational potential of a binary companion. They find that the tidal interactions for separations of ~ 200 inner disc radii (~ 2000 au in reality) warp the accretion disc of the YSO, resulting in disc, and therefore jet, precession. Considering the high companion fraction observed towards massive stars (see section 3.5 of Duchêne & Kraus 2013, and references therein), we might expect jet precession to be a relatively common phenomenon. Interestingly, their simulations also predict variable accretion and outflow rates that would be seen in observations as flux variability (Scaife et al. 2011), an effect recently observed towards a $20 M_{\odot}$ MYSO (Caratti O Garatti et al. 2017).

Radio observations of both variability and precession of massive jets are present in the literature, but are few and far in between. For example, Rodríguez et al. (2008) observed the MYSO IRAS 16547–4247 at two epochs separated by ~ 1000 d. From comparison of the flux maps in both epochs, no proper motions along the outflow axis were seen; however, precession was apparent in the non-thermal lobes with a rate of 0.08 yr^{-1} and therefore a derived period of < 4500 yr. Both the central jet and a non-thermal lobe (component S-1) increased in flux over time by 9 per cent and 36 per cent, respectively. As far as proper motion observations are concerned, several works have reported radio-lobe velocities ranging from 300 to 1000 km s^{-1} in massive cases (such as HH 80-81 and Cep A HW2 from Martí, Rodríguez & Reipurth 1998; Curiel et al. 2006, respectively).

Considering the discussion above, this work aims to investigate how ionized jets change over time. Specifically, we examine their flux variability, precession, and proper motions. To do this, we build upon the results of a previous survey of ionized jets (Paper I) that was based upon a well-selected sample of MYSOs from the RMS (Red MSX Source) survey (Lumsden et al. 2013). In that work, 26 ionized jets were detected from a sample of 49 objects, of which 11 of the 26 were associated with non-thermal emission. Using a new set of radio observations towards 4 of these 11 sources, this work increases the sensitivity by a factor of 2–3 ($\sim 10 \mu\text{Jy beam}^{-1}$) in comparison to Paper I. Specific questions we aim to answer are, do the radio jets exhibit variability over the period of time between observations (~ 2 yr)? Despite these short time baselines, can we still detect large proper motions towards the jets? Do they show precession in their propagation axes? Is there any fainter emission previously undetected? In light of answers to the previous questions, can we further constrain models of massive star/jet formation?

2 SAMPLE AND OBSERVATIONS

As mentioned above, four MYSOs associated with ionized jets were chosen from the sample of Paper I to be re-observed. These objects were selected on the basis of the presence of shock-ionized lobes, for which proper motions could be investigated, as well as a thermal jet centred on the MYSO. A range in bolometric luminosities are present across the four objects, and the lowest luminosity object (G263.7434+00.1161) was included on the basis of its hour angle, which allowed it to be observed at times when the rest of the sample were inaccessible. Further to this, its bolometric luminosity is typical of intermediate-mass objects and therefore its inclusion in the sample also allows for the investigation of this transition region from low-mass to high-mass regimes.

All radio observations were made using the Australian Telescope Compact Array (ATCA) in the 6A configuration, on 2014 December 19, 20, and 21. For reference, the observations of Paper I were conducted from 2013 February 25 to 28. A total of four individual objects were observed at two different frequency bands (centred on 6.0 and 9.0 GHz). These frequencies were observed using a bandwidth of 2048 MHz (XX, YY, XY, and YX polarizations) split evenly either side of the central frequencies, which was subsequently divided into 1 MHz channels. From this point on, the observed frequencies are referred to as the 6 and 9 GHz bands.

The ranges of scales the instrument was sensitive to were 1.8–18.5 and 1.2–12.3 arcsec for the 6 and 9 GHz frequency bands, respectively, corresponding to a minimum baseline length of 337 m and a maximum of 5939 m. Differing scale sensitivities can manifest in the results by a decrease in the amount of flux recovered at higher frequencies (i.e. on larger spatial scales). Paper I conducted synthetic observations towards an idealized jet model, representative of their sample in both spatial scale and spectral index. That investigation showed that for the ATCA in the 6A configuration, > 92 per cent of the flux was recovered at 6 and 9 GHz, and the recovered spectral index did not vary from the idealized model. Thus, these effects can be neglected in the further analysis of this paper. Furthermore, the synthetic observations showed that the signal-to-noise ratio was insufficient to accurately recover the physical dimensions of the object. However, with the deeper integration times of this data set, more accurate dimensions should be deconvolved from the data.

Scan times on the flux calibrator, phase calibrators, and science targets were 8, 2, and 15 min, respectively. In order to provide more coherent phase solutions between the two epochs, therefore increasing the reliability of image comparison and analysis, the phase calibrators were the same quasars as those used in Paper I. For the flux calibrator, an absolute flux scale uncertainty of 5 per cent is adopted for both frequencies. Listed in Tables 1 and 2 are the observed calibrators and science targets.

For reducing the data, the Multichannel Image Reconstruction, Image Analysis and Display (MIRIAD) software package (Sault, Teuben & Wright 1995) was used.

In the event that methanol masers or bright ($> 10 \text{ mJy}$) continuum sources were present in the field of view, phase-only (due to ATCA’s limited number of baselines) self-calibration was iteratively performed until no further improvement in the rms scatter of the phase solutions was achieved.

3 RESULTS

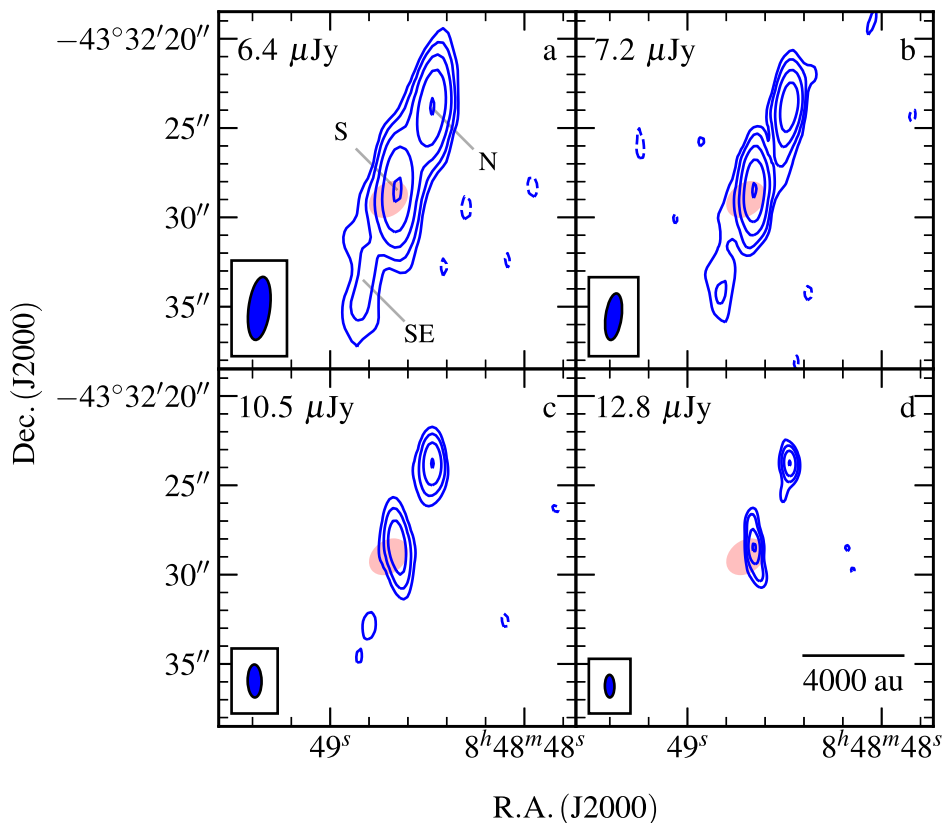
Maps of radio flux towards each of the four objects in our sample are shown in Figs 1–5 with separate clean maps produced at each frequency and each utilized robustness of -1 (improved resolution, reduced effects from residual sidelobes) and 0.5 (increased flux/large-scale sensitivity). Any channels displaying strong maser emission in the 6 GHz band were imaged and the positions of the brightest maser spot plotted as a green cross in the relevant contour plots. Values for the integrated fluxes (derived using the CASA task *imfit*), spectral indices (α), and power-law coefficient for the variation of the deconvolved major-axis length with frequency (γ) are presented in Table 3 for each identified radio lobe. In each case, the robustness of the clean maps used to derive these quantities is listed, with spatially distinct lobes generally utilizing a natural robustness and more confused sources making use of the enhanced resolution of the more uniformly weighted clean map (at the cost of increased noise).

Table 1. A table of the positions, calibration types, and fluxes for the calibrators used in the reduction of the data. In the final column, the science target(s) listed are the sources to which the complex gain solutions are transferred to, from the relevant phase calibrator (first column).

Calibrator	RA (J2000)	Dec. (J2000)	Type	Freq. (GHz)	S_ν (Jy)	Science target(s)
0826–373	08 ^h 28 ^m 04 ^s .78	−37°31′06″.3	Phase	6 9	1.55 ± 0.09 1.30 ± 0.10	G263.7434
1352–63	13 ^h 55 ^m 46 ^s .63	−63°26′42″.6	Phase	6 9	1.22 ± 0.14 1.08 ± 0.29	G310.0135, G310.1420, G313.7654
1934–638	19 ^h 39 ^m 25 ^s .03	−63°42′45″.6	Bandpass, flux	6 9	4.51 ± 0.35 2.72 ± 0.16	

Table 2. A table of the target sources, their positions, associated IRAS sources, distances, bolometric luminosities, ZAMS stellar masses (from the models of Davies et al. 2011, assuming a 30 per cent error in L_{bol}), total integration times, and theoretical image noise levels per beam (utilizing a robustness of 0) at 6 and 9 GHz.

Object	RA (J2000)	Dec. (J2000)	IRAS	D (kpc)	L_{bol} (L_\odot)	M_\star (M_\odot)	τ_{int} (h)	σ_6 (μJy)	σ_9 (μJy)
G263.7434+00.1161	08 ^h 48 ^m 48 ^s .64	−43°32′29″.0	08470–4321	0.7	1.2×10^3	$6.3^{+0.6}_{-0.2}$	7.33	7.3	8.4
G310.0135+00.3892	13 ^h 51 ^m 37 ^s .85	−61°39′07″.5	13481–6124	3.2	6.7×10^4	$24.3^{+3.1}_{-3.2}$	6.19	7.9	9.1
G310.1420+00.7583A	13 ^h 51 ^m 58 ^s .27	−61°15′41″.7	13484–6100	5.4	8.0×10^3	$11.2^{+1.0}_{-1.2}$	2.99	11.4	13.1
G313.7654–00.8620	14 ^h 25 ^m 01 ^s .53	−61°44′57″.6	14212–6131	7.8	6.1×10^4	$23.4^{+2.7}_{-3.0}$	5.29	8.6	9.9

**Figure 1.** Contour plots of radio flux density for observations made towards G263.7434+00.1161. rms noise is marked in the top left of each of the sub-plots that are as follows. (a) Image of 6 GHz data using a robustness of 0.5 where contours are $(-3, 3, 7, 15, 35, 79) \times \sigma$. (b) Image of 9 GHz data using a robustness of 0.5 where contours are $(-3, 3, 7, 15, 35, 78) \times \sigma$. (c) Image of 6 GHz data using a robustness of -1 with contours located at $(-3, 3, 7, 18, 42) \times \sigma$. (d) Image of 9 GHz data using a robustness of -1 with contours located at $(-3, 3, 7, 15, 33) \times \sigma$. Restoring beams are indicated in the bottom-left corner of each plot and are $3.55 \text{ arcsec} \times 1.20 \text{ arcsec}$ at $\theta_{\text{PA}} = -7^\circ.48$, $2.62 \text{ arcsec} \times 0.89 \text{ arcsec}$ at $\theta_{\text{PA}} = -7^\circ.76$, $1.84 \text{ arcsec} \times 0.78 \text{ arcsec}$ at $\theta_{\text{PA}} = 1^\circ.07$, and $1.27 \text{ arcsec} \times 0.53 \text{ arcsec}$ at $\theta_{\text{PA}} = 0^\circ.98$ for sub-plots (a), (b), (c), and (d), respectively. The 3σ positional error ellipse for the MSX point source associated with the MYSO is plotted in red.

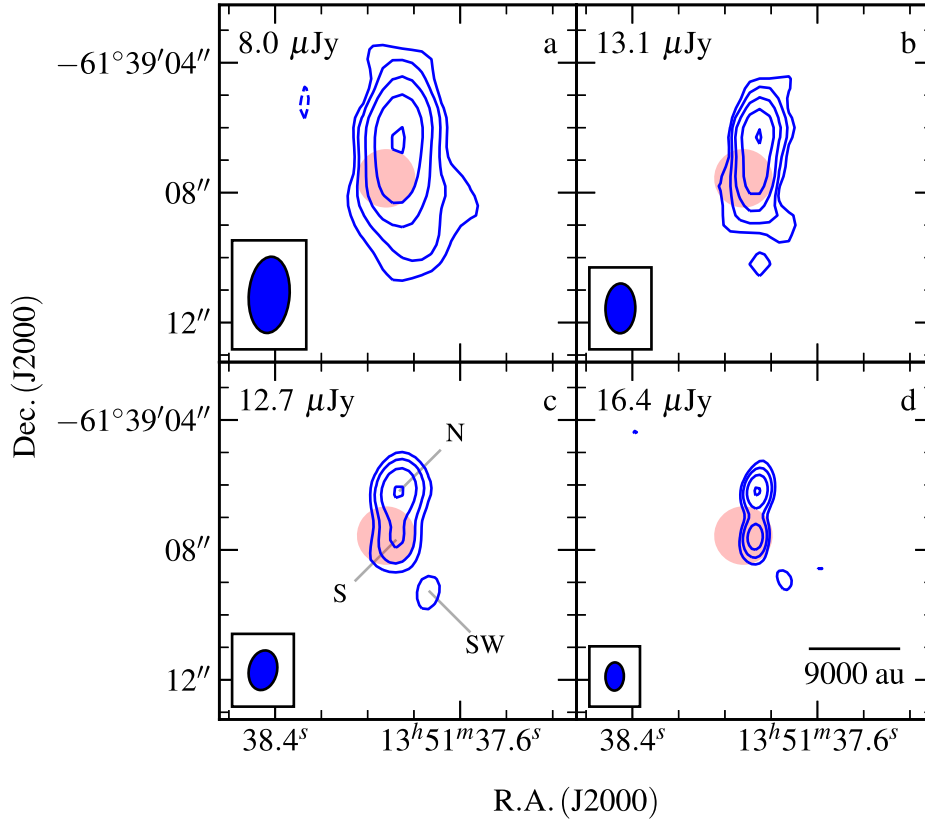


Figure 2. Contour plots of radio flux density for observations made towards G310.0135+00.3892. rms noise is marked in the top left of each of the sub-plots that are as follows. (a) Image of 6 GHz data using a robustness of 0.5 where contours are $(-4, 4, 9, 20, 44, 97) \times \sigma$. (b) Image of 9 GHz data using a robustness of 0.5 where contours are $(-4, 4, 8, 14, 27, 52) \times \sigma$. (c) Image of 6 GHz data using a robustness of -1 with contours located at $(-4, 4, 9, 21, 49) \times \sigma$. (d) Image of 9 GHz data using a robustness of -1 with contours located at $(-4, 4, 8, 17, 36) \times \sigma$. Restoring beams are indicated in the bottom-left corner of each plot and are $2.35 \text{ arcsec} \times 1.25 \text{ arcsec}$ at $\theta_{\text{PA}} = -4^\circ 43'$, $1.53 \text{ arcsec} \times 0.92 \text{ arcsec}$ at $\theta_{\text{PA}} = -1^\circ 13'$, $1.23 \text{ arcsec} \times 0.87 \text{ arcsec}$ at $\theta_{\text{PA}} = -12^\circ 29'$, and $0.87 \text{ arcsec} \times 0.57 \text{ arcsec}$ at $\theta_{\text{PA}} = -1^\circ 84'$ for (a), (b), (c), and (d), respectively. The 3σ positional error ellipse for the MSX point source associated with the MYSO is plotted in red.

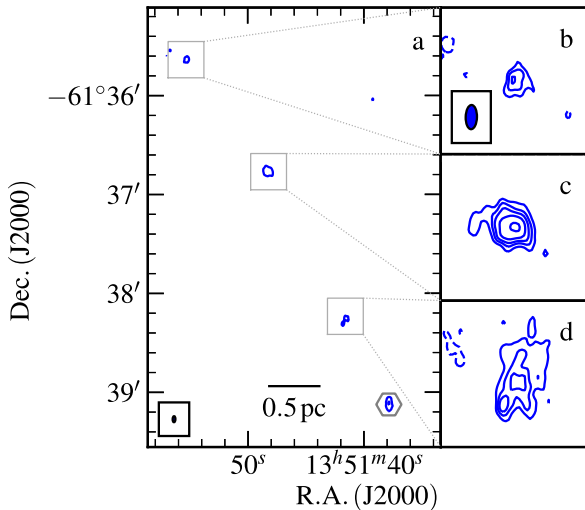


Figure 3. Primary beam-corrected 6GHz image (robustness of 2) of G310.0135+00.3892 and its associated radio Herbig-Haro objects. Each plot is (a) the overall area presented with 4σ and 50σ contours where $\sigma = 17.1 \mu\text{Jy beam}^{-1}$ with G310.0135+00.3892 is located in the bottom right (hexagonal marker). (b) Sub-plot of HH3 ($\sigma = 17.1 \mu\text{Jy}$). (c) Sub-plot of HH2 ($\sigma = 13.3 \mu\text{Jy}$). (d) Sub-plot of HH1 ($\sigma = 10.4 \mu\text{Jy}$). Contours are set at $(-3, 3, 5, 7, 10, 15) \times \sigma$ and the field of view is 22 arcsec, for (b), (c), and (d).

We now move on to give brief reviews of previous observations and discuss the results of the 2014 images, on an object-by-object basis.

3.1 G263.7434+00.1161

G263.7434+00.1161 is the nearest and lowest luminosity object in our sample, located in the Vela molecular ridge cloud D at a distance of 0.7 pc. Observations at 1.2 mm by Massi et al. (2007) revealed an $18 M_{\odot}$ compact core (MMS12, 0.13 pc in size) peaking ~ 5 arcsec to the east of our pointing centre. This mm-core is coincident with ‘complex and intense’ H₂ emission at $2.12 \mu\text{m}$ (de Luca et al. 2007), indicative of collisional excitation of molecular hydrogen through shocks attributable to protostellar outflows (Wolfire & Konigl 1991). Paper I identified two radio sources, one centred on the MYSO’s position (S) and the other offset ~ 4 arcsec to the NW. Derived spectral indices were thermal ($\alpha = 0.4 \pm 0.2$) and non-thermal ($\alpha = -0.5 \pm 0.3$) for S and N, respectively.

Fig. 1 shows this work’s maps of radio flux towards G263.7434+00.1161. Three lobes of emission, N, S, and SE, are detected at both frequencies and aligned along a position angle of $\sim 158^\circ$. Most obviously in the more uniformly weighted images (panels c and d of Fig. 1), the thermal jet (S) is in fact elongated along a different axis than that running through all three components (see Section 5.3 for further discussion of

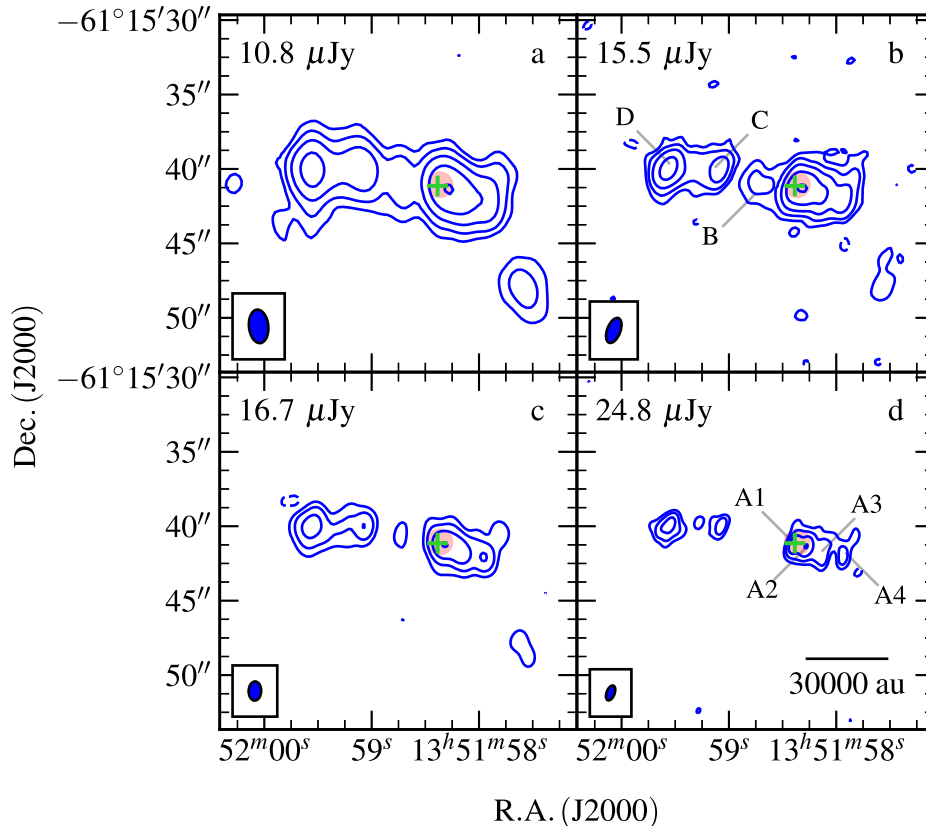


Figure 4. Contour plots of radio flux density for observations made towards G310.1420+00.7583A. rms noise is marked in the top left of each of the sub-plots that are as follows. (a) Image of 6 GHz data using a robustness of 0.5 where contours are $(-3, 3, 6, 13, 27, 58) \times \sigma$. The restoring beam was $2.26 \text{ arcsec} \times 1.30 \text{ arcsec}$ at $\theta_{\text{PA}} = 5^\circ 73$. (b) Image of 9 GHz data using a robustness of 0.5 where contours are $(-3, 3, 6, 13, 26, 54) \times \sigma$. The restoring beam was $1.77 \text{ arcsec} \times 0.89 \text{ arcsec}$ at $\theta_{\text{PA}} = -21^\circ 04$. (c) Zoomed-in image of 6 GHz data using a robustness of -1 with contours located at $(-3, 3, 7, 15, 32) \times \sigma$. The restoring beam was $1.28 \text{ arcsec} \times 0.84 \text{ arcsec}$ at $\theta_{\text{PA}} = -1^\circ 86$. (d) Zoomed-in image of 9 GHz data using a robustness of -1 with contours located at $(-3, 3, 6, 13, 27) \times \sigma$. The restoring beam was $1.05 \text{ arcsec} \times 0.54 \text{ arcsec}$ at $\theta_{\text{PA}} = -20^\circ 89$. The 3σ error ellipse in the position of the MSX point source is shown in red, while the detected methanol maser is shown as a green cross.

this). Component SE, whose peak is located ~ 4 arcsec from S at a position angle of $\sim 160^\circ$, is clearly elongated along a position angle of 178° with a length of ~ 5 arcsec (3500 au at a distance of 0.7 pc) and is calculated to possess a spectral index of 0.17 ± 0.68 . Approximately 29 arcsec to the south ($\alpha_{\text{J2000}} = 08^{\text{h}}48^{\text{m}}48^{\text{s}}.63$, $\delta_{\text{J2000}} = -43^\circ 32' 57''.8$), we detect a new source in both the 6 and 9 GHz clean maps that does not appear in the 2013 epoch's images (see Fig. B3 of Appendix B for a contour plot of radio flux), which we designate as S2. With integrated fluxes of 319 ± 28 and $363 \pm 31 \mu\text{Jy}$ at 6 and 9 GHz, it possesses a thermal spectral index of $\alpha = 0.32 \pm 0.30$ and has a GLIMPSE, mid-IR (MIR) counterpart.

3.2 G310.0135+00.3892

G310.0135+00.3892 (or IRAS 13481–6124) is well studied across a broad range of wavelengths. Kraus et al. (2010) used near-infrared (NIR) interferometric observations ($\theta_{\text{res}} = 2.4 \text{ mas}$ or 8.4 au at $\theta_{\text{PA}} = 114^\circ$) to directly observe a hot, dusty, compact ($13 \text{ au} \times 19 \text{ au}$) disc. Ilee et al. (2013) detected CO bandhead emission and subsequent modelling found temperature gradients consistent with the findings of Kraus et al. (2010) and with a flared, irradiated disc around a $21.8 M_\odot$ MYSO. The disc's major-axis orientation was found to be perpendicular to a collimated (opening angle $\sim 6^\circ$), CO, bipolar outflow (red lobe to the NE; Kraus et al. 2010), itself aligned

with two, $4.5 \mu\text{m}$ excesses (from inspection of IRAC imagery) separated by 6.5 pc , indicative of outflow activity. Corroborating these findings, diffraction-limited MIR imaging at $20 \mu\text{m}$ by Wheelwright et al. (2012) suggested that the dominant emission at $20 \mu\text{m}$ was from the walls of cavities evacuated by outflows along an NE–SW axis. Caratti o Garatti et al. (2015) observed the H_2 $2.122 \mu\text{m}$ transition, detecting lobes of emission spread over 6.9 pc at a position angle of -154° , parallel to the established molecular outflow. These lobes appeared to be more spread out to the NE (red lobe) showing that a density gradient exists in this direction. Paper I found three radio lobes associated with the MYSO designated as N, S, and SW with spectral indices of -0.2 ± 0.1 , 1.3 ± 0.2 , and 0.7 ± 1.7 , respectively. While the S and SW lobes are aligned to the general outflow direction, N is offset by $\sim 30^\circ$ to the west. It was deduced that while S represents the MYSO and base of the jet, the SW component is the faint thermal emission from the jet itself while N is likely optically thin and/or non-thermal emission as the result of wide-angle shocks from the jet on the surrounding material. The reason for the offset was unclear; however, Caratti o Garatti et al. (2016) observed spatially, and spectrally, resolved Br γ emission whose spatial velocity profile (their fig. 2) seemed to show a wide range in outflow angle, for a bipolar ionized jet with a terminal velocity of 500 km s^{-1} . This could possibly account for shock sites significantly deviating from the jet's outflow angle (26° according to Caratti o Garatti et al. 2015).

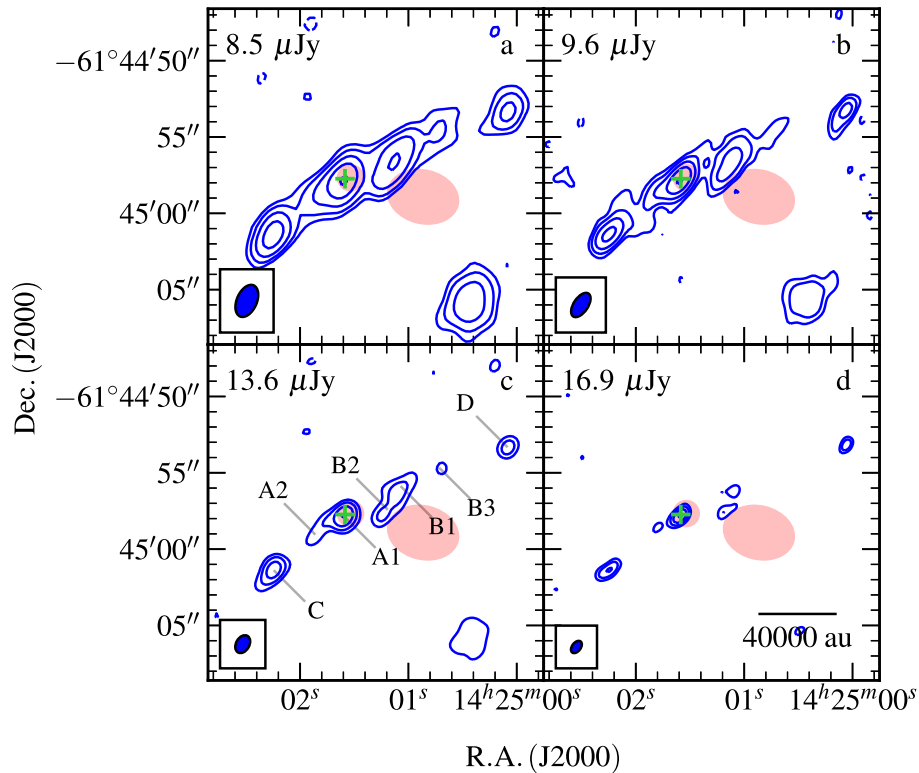


Figure 5. Contour plots of radio flux density for observations made towards G313.7654–00.8620. rms noise is marked in the top left of each of the sub-plots that are as follows. (a) Image of 6 GHz data using a robustness of 0.5 where contours are $(-3, 3, 6, 13, 27, 58) \times \sigma$. A restoring beam of $2.22 \text{ arcsec} \times 1.31 \text{ arcsec}$ at $\theta_{\text{PA}} = -23^\circ 69$ was used. (b) Image of 9 GHz data using a robustness of 0.5 where contours are $(-3, 3, 6, 13, 26, 54) \times \sigma$. A restoring beam of $1.80 \text{ arcsec} \times 0.95 \text{ arcsec}$ at $\theta_{\text{PA}} = -33^\circ 80$ was used. (c) Zoomed-in image of 6 GHz data using a robustness of -1 with contours located at $(-3, 3, 7, 15, 32) \times \sigma$. A restoring beam of $1.25 \text{ arcsec} \times 0.87 \text{ arcsec}$ at $\theta_{\text{PA}} = -29^\circ 68$ was used. (d) Zoomed-in image of 9 GHz data using a robustness of -1 with contours located at $(-3, 3, 6, 13, 27) \times \sigma$. A restoring beam of $0.91 \text{ arcsec} \times 0.57 \text{ arcsec}$ at $\theta_{\text{PA}} = -37^\circ 09$ was used. Both MSX (larger) and GLIMPSE error ellipses (smaller) are shown in red. A green cross marks the position of a detected methanol maser.

In the clean maps presented in Fig. 2, the previously established N, S, and SW components are detected at both frequencies. The SW lobe appears to ‘break up’ into two separate components from 6 to 9 GHz (comparing panels a and b of Fig. 2), separated by 1.4 arcsec. However, this may be due to image defects caused by strong, residual, sidelobes from a $\sim 27 \text{ mJy}$ source $\sim 470 \text{ arcsec}$ to the NW of the pointing centre. Imaging the whole of the primary beam at 6 GHz also shows three extended lobes of emission, designated as HH1, HH2, and HH3 (shown in Fig. 3, with positions recorded in Table A2 of Appendix A). These sources lie at separations of 0.88, 2.47, and 3.78 pc with position angles of 30° , 27° , and 31° from the MYSO, respectively. No spectral indices could be computed since 9 GHz clean maps resolved out much of the extended emission of these lobes.

3.3 G310.1420+00.7583A

G310.1420+00.7583A is associated with IRAS 13484–6100 and is offset by $\sim 8 \text{ arcsec}$ from a cometary UCHII (G310.1420+00.7583B). The radio observations of Paper I detected seven separate components, named A1 (MYSO), A2, A3, A4, B, C, and D, roughly aligned east to west with a total, integrated flux of $\sim 10 \text{ mJy}$. Previous to that, Urquhart et al. (2007) detected radio emission (observations conducted in 2004 November) at 4.8 GHz coincident with components A1 and A2, with an integrated flux of $2.92 \pm 0.75 \text{ mJy}$ (fitted from the archived image using *imfit*). Different masing species have been detected towards this source

(OH, H₂O, and CH₃OH: Walsh et al. 1998; Urquhart et al. 2009; Green et al. 2012, respectively), with the methanol maser coincident (multibeam survey positional accuracy is $< 0.1 \text{ arcsec}$) with A1. Caratti o Garatti et al. (2015) observed two knots of H₂ emission, one of which also displayed Br γ emission indicative of strong dissociative shocks (their ‘knot 1’ or D of Paper I) with shock velocities $> 90 \text{ km s}^{-1}$ within a medium of density $\sim 10^5 \text{ cm}^{-3}$. Jet properties inferred from the H₂ observations included a length of 0.4 pc, precession of 17° , and electron density, n_e , of $(4 \pm 1) \times 10^4 \text{ cm}^{-3}$. An extended green object (EGO) was also detected offset from knot 1 by $\sim 16 \text{ arcsec}$ at a position angle of 57° (Cyganowski et al. 2008).

The clean maps shown in Fig. 4 show all components detected by Paper I aligned in a jet-like morphology along a position angle of $\sim 78^\circ$. One previously undetected component is seen at the 6σ level (panel a), located $\sim 5.5 \text{ arcsec}$ to the east of component D. At 9 GHz, it is not detected and an upper limit to the spectral index of $\alpha < 0$ is derived from the peak flux at 6 GHz. We also detect radio emission roughly connecting lobe C to D, which is especially well shown in panels (b) and (c) of Fig. 4, and methanol maser emission coincident with A1. Fluxes and positions for A1, A2, A3, and A4 proved difficult to measure via *imfit* due to source confusion. Using clean maps with a robustness of 0.5, the emission from A1 and A2 could not be separated and only at 9 GHz, using a robustness of -1 , could we deconvolve each individually. For components B, C, and D, this was not the case and consequently sizes and integrated fluxes are derived from the clean map with a robustness of 0.5 to maximize the signal-to-noise ratio. A resolved-out H II region is also seen to

Table 3. A table of the integrated fluxes (whose errors take into account a 5 per cent absolute flux error at 6 and 9 GHz), derived spectral indices for flux (α), and major-axis length (γ), for all objects in the 2014 epoch observations.

Name	Comp.	S_6 (μJy)	S_9 (μJy)	α	θ_{maj}^6 (arcsec)	θ_{maj}^9 (arcsec)	γ	R
G263.7434+00.0161	N	626 \pm 43	594 \pm 44	-0.13 \pm 0.25	1.40 \pm 0.19	1.40 \pm 0.14	-0.01 \pm 0.41	0.5
	S2	319 \pm 28	363 \pm 31	0.32 \pm 0.30	1.13 \pm 0.49	1.04 \pm 0.27	-0.20 \pm 1.25	0.5
	S	767 \pm 52	837 \pm 58	0.22 \pm 0.24	2.24 \pm 0.13	1.85 \pm 0.10	-0.47 \pm 0.19	0.5
	SE	126 \pm 22	135 \pm 29	0.17 \pm 0.68	5.18 \pm 1.09	5.29 \pm 1.27	0.05 \pm 0.79	0.5
G310.0135+00.3892	N	707 \pm 53	695 \pm 66	-0.04 \pm 0.30	0.28 \pm 0.07	-	-	-1
	S	347 \pm 37	481 \pm 53	0.81 \pm 0.38	0.50 \pm 0.16	-	-	-1
	SW	126 \pm 35	93 \pm 32	-0.75 \pm 1.09	<2.60	-	-	-1
G310.1420+00.7583A	A1	}2744 \pm 177	1459 \pm 122	-	}0.84 \pm 0.03	0.66 \pm 0.28	-	-1
	A2		1852 \pm 147	-		0.62 \pm 0.06	-	-1
	A3	2053 \pm 144	1295 \pm 160	-1.14 \pm 0.35	1.09 \pm 0.04	1.36 \pm 0.14	0.53 \pm 0.28	-1
	A4	888 \pm 83	570 \pm 94	-1.09 \pm 0.47	0.93 \pm 0.10	1.00 \pm 0.22	0.18 \pm 0.60	-1
	B	205 \pm 65	117 \pm 61	-1.38 \pm 1.50	2.78 \pm 0.94	-	-	-1
	C	568 \pm 56	511 \pm 74	-0.26 \pm 0.43	<0.51	0.50 \pm 0.17	> -0.03 \pm 0.82	-1
	D	1896 \pm 137	1684 \pm 157	-0.29 \pm 0.29	1.09 \pm 0.05	0.98 \pm 0.08	-0.25 \pm 0.22	-1
G313.7654-00.8620	A1	506 \pm 46	537 \pm 55	0.15 \pm 0.34	<0.57	0.43 \pm 0.10	> -0.67 \pm 0.60	-1
	A2	183 \pm 39	170 \pm 60	-0.18 \pm 1.02	<3.00	1.92 \pm 0.76	> -1.10 \pm 0.98	-1
	B1	350 \pm 54	240 \pm 76	-0.93 \pm 0.87	1.74 \pm 0.25	1.92 \pm 0.62	0.24 \pm 0.87	-1
	B2	116 \pm 27	167 \pm 46	0.90 \pm 0.89	-	1.20 \pm 0.41	-	-1
	B3	118 \pm 30	81 \pm 27	-0.93 \pm 1.03	2.15 \pm 0.90	1.97 \pm 1.11	-0.22 \pm 1.73	0.5
	C	420 \pm 44	399 \pm 57	-0.13 \pm 0.44	0.85 \pm 0.12	1.06 \pm 0.15	0.53 \pm 0.50	-1
	D	138 \pm 25	157 \pm 28	0.32 \pm 0.62	-	-	-	-1
	F	85 \pm 22	85 \pm 25	0.00 \pm 0.97	<2.2	-	-	0.5
G	171 \pm 59	51 \pm 18	-2.98 \pm 1.02	4.75 \pm 1.56	-	-	0.5	

the south west of A1 (RMS survey alias G310.1420+00.7583B or component E from Paper I), which is not discussed further.

3.4 G313.7654-00.8620

Associated with IRAS 14212-6131, the observations of Paper I detected six associated radio components named A1 (MYSO), A2, B1, B2, C, and D. Both hydroxyl (Caswell 1998) and methanol (Green et al. 2012) masers have been previously observed, the latter of which was separated from A1 by ~ 1 arcsec at a position angle of 108° . Caratti o Garatti et al. (2015) detected four knots of H_2 emission that, if tracing a jet, show evidence of a precession in the jet's axis of 32° . Knot 1 (coincident with B1 of Paper I) has an inferred electron density of $(1 \pm 0.5) \times 10^4 \text{ cm}^3$, while knot 4 (most distant) displays Br γ emission indicative of strong J-type shocks with a shock speed of $\sim 60 \text{ km s}^{-1}$. Currently, the jet axis is defined at a position angle of 125° , with a length (on one side) of 1.4 pc. GLIMPSE images show diffuse $4.5 \mu\text{m}$ excesses in the general area of previously established radio emission, an extended H II region ~ 30 arcsec to the west, and a compact H II region ~ 10 arcsec to the south west (E from Paper I).

Two new components are seen in the clean maps of Fig. 5 compared to Paper I. One is situated ~ 2 arcsec to the NW of B1, which we designate as B3, and the other approximately halfway between A2 and C, which is relatively diffuse and is therefore unnamed. For B3, we derive a spectral index of $\alpha = -0.9 \pm 1.0$. Outside the clean maps of Fig. 5, a radio source (shown in Fig. B4 in the online version) is detected ~ 24 arcsec to the NE of A1, named F, for which we measure integrated fluxes of 85 ± 18 and $85 \pm 21 \mu\text{Jy}$ at 6 and 9 GHz, respectively, and derive $\alpha = 0.0 \pm 1.0$. It is also interesting to note that there is an extended radio lobe with spectral index $\alpha = -3 \pm 1$ (suffering from resolving-out effects at 9 GHz) detected ~ 33 arcsec from A1 at $\theta_{\text{PA}} \sim -81^\circ$, which we name G.

Two 6.7 GHz methanol maser spots are also detected, one coincident with A1 (see Fig. 5) and the other coincident with F. For the calculation of spectral indices, a robustness of -1 was employed at all frequencies to allow for the effective deconvolution and subsequent measurement of all component's (apart from B3) integrated fluxes. Component B3 was only detected in the clean maps with a robustness of 0.5 but was sufficiently separated from B1/B2 to allow the accurate deconvolution and measurement of its flux. For all lobes, calculated spectral indices agree with the values obtained in Paper I.

4 NECESSARY CONSIDERATIONS

Prior to the analyses conducted in Section 5, two issues affecting the direct comparison of images from different epochs required careful consideration. In the rest of this section, we highlight their implications upon our analyses, and our approach to negate, or at least accommodate for, their effects.

4.1 Image alignment

Measurement of the positional changes of radio lobes over subsequent observations allows for the direct measurement of the ionized gas' velocity (in the plane of the sky). In order to do this, accurate positional measurements are required due to the great distances involved, particularly for our sample that has relatively short time baselines. For example, with two measurements separated by a period of 2 yr, assuming a jet velocity of 500 km s^{-1} for a distance of 3 kpc, we expect an angular shift (assuming that the jet's path lies in the plane of the sky) of 0.07 arcsec. However, due to imperfections in calibration, as well as astrometric inaccuracy, coordinates have an absolute positional uncertainty. In an effort to negate this effect, we used the same phase calibrators for our new observations as for

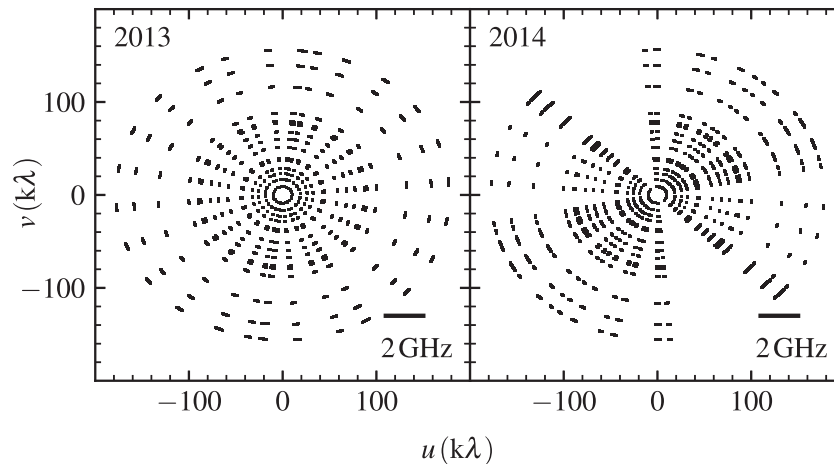


Figure 6. Plots of the sampling functions (single channels at 9 GHz) for the 2013 and 2014 data sets towards G310.1420+00.7583A. Illustrated in the bottom right of each plot is a scale bar showing the radial uv -coverage over the 2 GHz bandwidth (6 km baseline).

those of 2013. Extragalactic background sources were subsequently identified from the clean maps of radio flux (on the basis of spectral index and lack of IR counterparts), and any positional shift of these objects between the two images was assumed to be due to positional errors. This provided corrections that were applied to the 2014 images using spline interpolation, therefore aligning the two images with subsequent analyses utilizing these ‘corrected’ clean maps.

4.2 Variable ATCA flux recovery

Different sampling of the uv -plane for each of the two epochs can change recovered flux densities, distributions, and morphologies. To investigate the effects this difference has on the resulting clean maps, a set of synthetic observations were created mirroring both the system temperatures and sampling functions, $S(u, v)$, of the 2013 and 2014 data (shown in Fig. 6) taken towards one of our targets (G310.1420+00.7583A). This particular object was chosen on the basis of its complex morphology that contains both separate and spatially confused emission. The model chosen was one identical to the (*imfit*-derived) positions, integrated fluxes, and sizes recorded in the 2013 data of the six most prominent lobes (A1, A2, A3, A4, C, and D). Resulting clean maps and pixel-to-pixel flux difference maps are presented in Figs B1 and B2, respectively, of Appendix B (online version only). The subsequent analysis of these synthetic data showed that relative gaps in uv -coverage have acted to decrease the amount of recovered flux from 2013 to 2014 by -16 per cent. Predictably, this effect is amplified for the more extended components, C and D, but the negative percentage change is apparently greater for A3 (a relatively compact lobe). Further to this, the integrated flux actually increases for A2 in both epochs. Both of these effects however are not solely due to the differing synthetic apertures, but also due to the inaccuracy of fitting multiple, closely spaced, Gaussian distributions of flux. This is reflected again in the inability of the 2014 synthetic observations to deconvolve A2 as a point source (as in the model), and subsequently it was measured to have finite angular size and position angle. Component A4 also appears to significantly relocate by ~ 0.19 arcsec, at a position angle of -16° , for the 2014 data set compared to the model. This is equivalent to a proper motion-derived velocity of ~ 2900 km s $^{-1}$ for G310.1420+00.7583A’s distance of 5.4 kpc. In summary, we can say the following.

- (i) Fluxes recovered by the synthetic observations are on average -11 per cent and -25 per cent lower than actual values supplied by the model, with extended sources C and D affected worst.
- (ii) Percentage of flux recovered for the 2014 observations is lower than for the 2013 observations, whereby, on average, 16 per cent less flux is recovered per component.
- (iii) Source confusion leads to the wrong distribution of flux for lobes A2 and A3, with the compact source A2 ‘leeching’ flux from A3.
- (iv) Lobe positions are deduced with better than 0.1 arcsec accuracy in non-source confused components.
- (v) Position angles for the emission are relatively well recovered by *imfit*, with average deviations of just -2° and 6° (ignoring source confused lobes, A2 and A3) for the former and latter epochs, respectively.

This analysis implies that for complex sources such as G310.1420+00.7583A and G313.7654–00.8620, any proper motions < 0.1 arcsec are likely to be too affected by poor uv -coverage and source confusion to draw any conclusions from. Negative variations over time in integrated lobe fluxes between 2013 and 2014 should be regarded with caution. Pixel-to-pixel comparisons of the maps of flux also show non-real negative flux variations centred on components A1, A2, A3, and A4. These considerations are therefore necessarily taken into account for the rest of this work.

5 DISCUSSION

Observations presented in Section 3 have detected new radio emission towards a small sample of YSOs across a range in bolometric luminosity. We now move on to discuss our results and their implications upon the natures of newly detected faint emission, the variability/proper motions of the jets and their lobes, and precession in the jets’ outflow axes.

5.1 Natures of newly detected emission

Towards all of the objects in the sample, apart from G310.1420+00.7583A, sources of radio emission below the detection threshold of previous observations are detected, resulting from many different processes.

In the case of G263.7434+00.1161’s SE component, morphology of the emission at 6 GHz shows it to be extended in a jet-like,

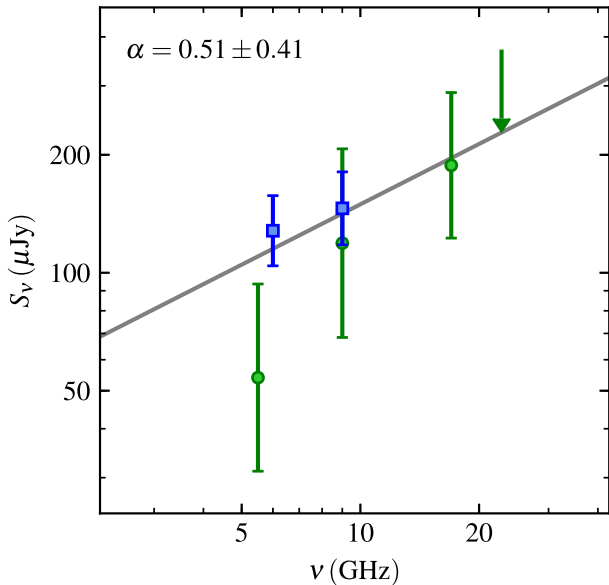


Figure 7. A plot of integrated flux against frequency for the SE component of G263.7434+00.1161. Green circles and blue squares represent data from Paper I and this work, respectively, with the upper limit being that of the 22.8 GHz data from Paper I. All error bars shown include a 5 percent uncertainty in the absolute flux calibration. The grey line shows the (log-space) weighted, least-squares fit of the combined data from both epochs, with the derived spectral index shown in the top-left corner.

elongated structure (5.2×0.6) arcsec at a position angle of 179° . However, the spectral index derived from 6 to 9 GHz ($\alpha = 0.17 \pm 0.68$) was unable to establish whether it was thermal or non-thermal in nature. In an attempt to constrain the emission processes at work, the data from Paper I were re-imaged with a robustness of 2 (in order to maximize sensitivity) and a 3σ component was detected, coincident with the new SE lobe, at 5.5, 9, and 17 GHz. Least-squares fitting to the first epoch’s data alone yields a spectral index of 1.06 ± 0.61 , while for the combined fluxes of all available data, a spectral index of $\alpha = 0.51 \pm 0.41$ is calculated (see Fig. 7). This value for the spectral index (0.51 ± 0.41) determines it to be the direct, thermal emission from the jet’s stream and is compatible with a wide variety of scenarios from the models of Reynolds (1986), including the ‘standard’ spherical case of a freely flowing ionized jet. Considering its properties and alignment with the north–south component axis, this likely represents the fainter, direct, thermal emission from the jet’s stream. A discussion of the new radio object, S2, detected 29 arcsec to the south of G263.7434+00.1161 is reserved for Section 5.2.

With G310.0135+00.3892, in comparison to other objects in this sample, the previously undetected emission (HH1, HH2, and HH3) is found to be greatly separated from the MYSO itself (up to 3.78 pc) but still roughly aligned along the same axis of $\sim 30^\circ$ with respect to S, much like the HH 80–81 system (which has Herbig–Harro objects spread over 5.3 pc; Marti et al. 1993). In comparison with a previous NIR study (Caratti o Garatti et al. 2015), HH1, HH2, and HH3 are spatially coincident with their 2.122 μm , H₂ lobes ‘E red’, ‘D red’, and ‘bow shock A red’. Considering that this type of emission is the result of shocks with velocities $> 15 \text{ km s}^{-1}$ (Elias 1980), this confirms HH1, HH2, and HH3’s status as radio Herbig–Harro lobes. From their integrated fluxes and sizes, average emission measures of 5350 ± 825 , 9590 ± 1250 , and $9990 \pm 2110 \text{ pc cm}^{-6}$ are calculated,

while average electron densities are found to be 303 ± 55 , 351 ± 61 , and $549 \pm 116 \text{ cm}^{-3}$ for HH1, HH2, and HH3, respectively.

An important point for discussion is the relatively asymmetric nature of the radio flux’s distribution towards G310.0135+00.3892, whereby the SW component has no corresponding NE lobe. We know from previous observations that a bipolar, collimated, ionized jet is present at both large and small scales (Caratti o Garatti et al. 2015, 2016, respectively; see Section 3.2), and therefore a monopolar jet is unlikely. With uncertain spectral indices, the SW component may arise from a variety of physical mechanisms. If the SW lobe was shocked emission from the jet impinging upon clump material, it could be a reflection of the asymmetry of its environment. Indeed, the distribution of H₂ shock emission seen by Caratti o Garatti et al. (2015) was postulated to be due to a higher density of material towards the SW, in comparison to the NE, a picture supported by the MYSOs offset of 7 arcsec to the NE of the peak position of its parental clump (Contreras et al. 2013). Alternatively, the presence of the accelerating flow (Caratti o Garatti et al. 2016) suggests largely evacuated outflow cavities and therefore the shock site may reside in the cavity walls. Finally, if SW is a shock internal to the jet, or indeed thermal emission from the jet’s stream, this could be due to asymmetric ejection in velocity and/or mass flux. Only further radio observations over longer time baselines could discern between these potential explanations.

Diffuse faint emission between the previously established lobes, A2 and C, of G313.7654–00.8620 was detected, which is likely ‘filling in’ the jet’s emission as a result of the increased sensitivity of this set of observations. Component F on the other hand is distinctly separated from the main radio emission, is compact, and has a methanol maser detected towards it meaning it is likely another MYSO in the vicinity. However, it has no clear NIR or MIR counterpart and therefore must be deeply embedded within the clump and/or relatively unevolved. Maps of 2.122 μm H₂ emission seen by Caratti o Garatti et al. (2015) show the other new radio component B3 to be coincident with their ‘knot 1’, a fact that, in conjunction with B3’s alignment to the presumed jet outflow axis, classifies it as a likely jet-shocked surface. Unfortunately, B3’s spectral index was calculated to be -0.9 ± 1.0 meaning the exact emission processes at work could not be constrained. Further from the obvious string of jet lobes is radio lobe G detected 33 arcsec to the west. Considering the relative position angle of the emission from the thermal jet (A1) and coincidence with an NIR H₂, 2.122 μm lobe (knot 4 of Caratti o Garatti et al. 2015), we propose this to be another surface upon which the jet of outflowing material is impinging. This position also sits at the head of a cometary H II region’s bow shock, from which extended, partially resolved-out emission is detected at 6 GHz. It is therefore possible that this new radio emission is attributable to the H II region and not with a shocked surface along the jet’s axis. However, archival observations, taken on 09/12/2011 at 2 GHz, show the H II region’s emission to be offset to the detected radio lobe (Fig. 8), and extended along a position angle of $\sim 95^\circ$ across an extent of ~ 10 arcsec (perpendicular to the MIR H II region’s ‘front’). Since the H II region at 2 GHz is not co-located with the radio lobe at 6 GHz, which itself is coincident with NIR shock emission, this lobe may still be attributable to jet activity.

5.2 Variability and proper motions

To examine both the flux variability and motion of radio sources, a comparison of both the *imfit*-derived lobe positions and integrated 9 GHz fluxes from Paper I with those recorded here was performed (tabulated in Table 4). Considering the short time baseline between

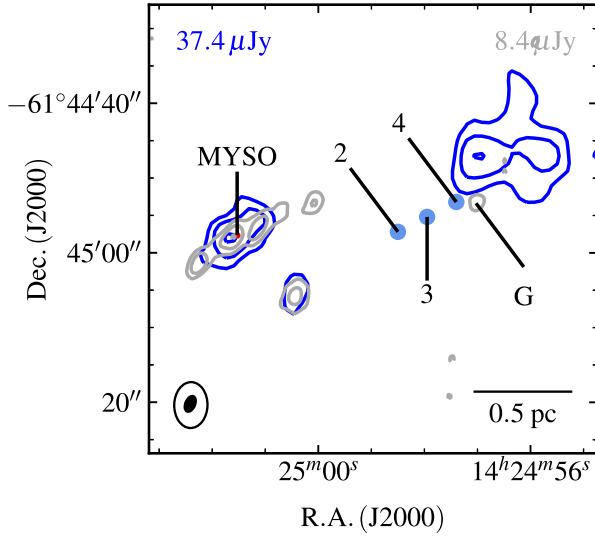


Figure 8. Radio contour map of the general area towards G313.7654–00.8620 utilizing a robustness of 0.5, at 2 GHz (blue contours) and 6 GHz (grey contours). Restoring beams are illustrated in the bottom-left corner and the 2 GHz beam has dimensions of $6.14 \text{ arcsec} \times 4.45 \text{ arcsec}$ at $\theta_{\text{PA}} = -1^{\circ}24$. Contours are set at $(-4, 4, 6, 10) \times \sigma$ and $(-4, 4, 15, 58) \times \sigma$ for the 2 and 6 GHz data, respectively. The value employed for σ is indicated in the top-left (for 2 GHz) and top-right corners (for 6 GHz). Filled, blue circles indicate the $2.12 \mu\text{m}$ knots, ‘knot 2’, ‘knot 3’, and ‘knot 4’ from Caratti o Garatti et al. (2015). The radio lobe detected at 6 GHz, which suggests an overall precession, in the outflow axis is annotated.

the two data sets, the 3σ lower limits (assuming $\sim 0.1 \text{ arcsec}$ positional uncertainty) on the proper motions are relatively high, ranging from 600 to 6000 km s^{-1} , and therefore realistically their detection was not expected.

From the *imfit*-measured 2013 and 2014 9 GHz fluxes, only two components directly attributable to the jets show significant ($>3\sigma$) variability, being component A2 of G310.1420+00.7583A and A2

of G313.7654–00.8620. However, since many of the sources’ flux distributions (especially these two) are not simple, it is unclear whether this change is due to inaccuracies in either deconvolution, measurement of the emission using *imfit*, or both. A pixel-to-pixel comparison and analysis helped to reveal that variability is likely present towards G310.1420+00.7583A, without relying on accurate deconvolution by a multiple set of Gaussians in the image plane. In Fig. 9, the absolute change in the flux for each pixel is plotted for G310.1420+00.7583A (Fig. 9) showing well-ordered variability towards the western side of the jet (i.e. A2, A3, and A4). However, as discussed in Section 4.2, this was an expected effect of differing sampling functions for the two sets of observations (comparing Fig. 9 to its synthetic equivalent in Fig. B2 of Appendix B). Unexpectedly, from considerations of *uv*-coverages, component D shows an increase in the pixel fluxes towards its peak flux position, not reflected in its integrated flux (via measurement with *imfit* or integrating flux within the 3σ contours). Therefore, we suggest that D is a spatially resolved shock site, which is evolving over time.

Away from the obvious emission along the ionized jets’ axes, a highly variable radio source (S2) was detected 29 arcsec to the south of G263.7434+00.1161 that should have been seen at the $\sim 12\sigma$ level in the 2013 data and as such possesses a lower limit on its 9 GHz flux change of $> 283 \pm 41 \mu\text{Jy}$. The thermal nature of the radio emission precludes extragalactic origins since only starburst galaxies rich in H II regions should display thermal spectral indices, but their fluxes should not be variable on the time-scale of $\sim 2 \text{ yr}$. At a position angle of 181° from S, which is roughly aligned with the deconvolved position angle of S’s major axis, it is possible that this source may be a highly variable radio Herbig–Haro object. On the other hand, it is separated by 0.17 arcsec (which is likely coincident within astrometric errors) from a 2MASS source (J08484864–4332578) that is likely to be a reddened main-sequence star and therefore may alternatively be a highly variable radio star. On the basis of these results however, no definitive classification could be made.

Table 4. A table of the proper motion-derived velocities/position angles and integrated flux changes from the first to second epochs. These quantities are calculated from the *imfit*-derived positions/fluxes at 9 GHz. Upper limits given are the 3σ upper limits. Velocities incorporate errors on distances of 1 kpc (i.e. spiral arm width) apart from G263.7434+00.1161, whose distance error is 0.2 kpc (Liseau et al. 1992).

Source	Lobe	r (arcsec)	v_{PM} (km s^{-1})	θ ($^{\circ}$)	ΔS_9 (μJy)	R
G263.7434+00.1161	N	0.032 ± 0.062	<339	29 ± 66	<270	0.5
	S	0.060 ± 0.032	<183	245 ± 63	<375	0.5
	SE	0.716 ± 0.388	<2208	241 ± 54	<276	0.5
	S2	–	–	–	$>283 \pm 41$	0.5
G310.0135+00.3892	N	0.101 ± 0.035	<1188	307 ± 24	<324	–1
	S	0.071 ± 0.052	<1431	346 ± 24	<276	–1
	SW	0.092 ± 0.140	<3582	338 ± 42	<219	–1
G310.1420+00.7583A	A1	0.097 ± 0.012	1376 ± 308	97 ± 26	<591	–1
	A2	0.115 ± 0.036	<1791	35 ± 13	933 ± 171	–1
	A3	0.238 ± 0.043	3371 ± 867	309 ± 12	<726	–1
	A4	0.453 ± 0.079	6409 ± 1627	351 ± 3	<505	–1
	B	0.318 ± 0.121	<5718	186 ± 8	<285	0.5
	C	0.128 ± 0.035	1806 ± 596	70 ± 26	<552	0.5
	D	0.068 ± 0.049	>2145	344 ± 16	<699	0.5
G313.7654–00.8620	A1	0.063 ± 0.020	<1320	244 ± 27	<321	–1
	A2	0.754 ± 0.149	$15\,404 \pm 3631$	309 ± 13	304 ± 82	0.5
	B1	0.196 ± 0.109	<6825	195 ± 17	<225	0.5
	B2	0.511 ± 0.100	$10\,444 \pm 2449$	327 ± 8	<135	0.5
	C	0.043 ± 0.104	<6363	161 ± 68	<372	–1
	D	0.110 ± 0.052	<3279	326 ± 24	<258	–1

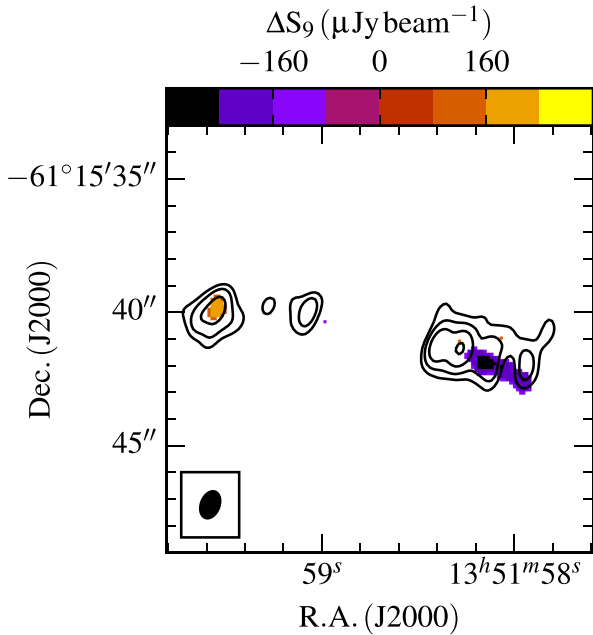


Figure 9. A plot of the absolute flux difference between the 2014 and 2013 9 GHz clean maps (robustness = -1) of radio flux for G310.1420+00.7583A (colour scale). Only the pixels whose flux difference was $\Delta S_v \leq -4\sigma$ | $\Delta S_v \geq 4\sigma$ were included (where $\sigma = 34.5 \mu\text{Jy beam}^{-1}$, the rms noise in the map of absolute flux difference). The common restoring beam's dimensions were $1.05 \text{ arcsec} \times 0.69 \text{ arcsec}$ at $\theta_{\text{PA}} = -20^\circ.9$. Contours represent the 9 GHz data taken in 2014 with -4, 4, 9, 21, and 47 σ shown ($\sigma = 22.4 \mu\text{Jy beam}^{-1}$).

With regard to lobe proper motions, only the morphologically complex sources (i.e. A1, A2, A3, and A4 of G310.1420+00.7583A and A2, B1, and B2 of G313.7654-00.8620) showed significant proper motions in the fitted positions for the lobes. Derived velocities for some of the lobes (i.e. $\sim 10^4 \text{ km s}^{-1}$ for B2 and A2 of G313.7654-00.8620) are extremely high and, considering typical, proper motion values in the literature (300-1000 km s^{-1} ; Martí, Rodríguez & Reipurth 1995; Rodríguez et al. 2008; Guzmán et al. 2010), likely due to errors during deconvolution and/or using the *imfit* task (as with flux variability). Towards G310.1420+00.7583A's lobe C (which is located away from differing *uv*-coverage effects) however, a more reasonable, and statistically significant, proper motion of $1806 \pm 596 \text{ km s}^{-1}$ is calculated. A derived position angle of $70^\circ \pm 26^\circ$ places the proper motion along the jet's propagation axis supporting the case that the observed motion is real. This is therefore the only radio lobe for which we reliably detect proper motions amongst the sample.

5.3 Precession

Various forms of evidence for precession are found towards all four objects of the sample with a large range in both derived precession periods and angles.

In the case of G263.7434+00.1161, the deconvolved position angles for the thermal jet (S) of $6^\circ \pm 2^\circ$, at both 6 and 9 GHz, suggest that the jet's current axis is offset by $35^\circ.7 \pm 1^\circ.6$ w.r.t. the axis running through N, S, and SE ($\theta_{\text{PA}} = -29^\circ.9 \pm 0^\circ.24$). Assuming a jet velocity of 500 km s^{-1} , $i = 90^\circ$, and N to be optically thin emission from jet material (or a shock) that was therefore ejected on a ballistic trajectory from S $33 \pm 10 \text{ yr}$ ago (assuming a distance error of 200 pc), a precession rate of $1^\circ.1 \text{ yr}^{-1}$ is estimated, much higher than precession rates for other ionized jets found in the literature.

The complex, $2.122 \mu\text{m}$, H_2 emission previously observed (fig. A9 of de Luca et al. 2007) could be the result of a jet with a high precession rate creating shock sites over a wide range in angles, over a relatively short period, or multiple sources. It must be conceded that YSO/outflow multiplicity is an alternative explanation for these results. However, assuming that this change in the jet axis' angle over 33 yr is a result of a binary interaction and half the total period, a separation of $30 \pm 6 \text{ au}$ is inferred for the companion. To calculate this orbital separation, we assume standard, Keplerian behaviour and employ the following equation:

$$r = \left(\frac{P^2 GM}{4\pi^2} \right)^{\frac{1}{3}}, \quad (1)$$

where P is period, M is the total mass of the binary system, and r is the orbital semi-major axis.

For G310.0135+00.3892, variations in the position angles of the Herbig-Haro radio lobes HH1, HH2, and HH3, with respect to S, are seen. Fitting the 6 GHz peak positions of these HH objects, and the SW component with a jet model, via minimization of χ^2 as described in Appendix C (with fixed values of $i = 42^\circ$ and $\theta_{\text{PA}} = 31^\circ$; Boley et al. 2016), yields a precession angle and period of $15480_{-2248}^{+3409} \text{ yr}$, respectively. Should this precession be due to a regular orbiting body, it should be separated by $1797_{-191}^{+275} \text{ au}$ from the MYSO. It must be noted that a precession angle and period of 8° and 8300 yr (inferring an orbital radius of 1200 au) fit the (limited) data equally as well, but a period of 15480 yr represents the simplest model. Since the position angle for the established HH jet lies at an angle of 29° , as discussed previously, the exact nature of the lobe N is an open question since it lies at a position angle of -3° from the MYSO/thermal jet at S. If N is an optically thin H II region, on the basis of its radio flux (and assuming a distance of 3.2 kpc), a bolometric luminosity of $\sim 4000 L_\odot$ (ZAMS type B2; Davies et al. 2011) is implied, with a calculated average emission measure of $\sim 7 \times 10^6 \text{ pc cm}^{-6}$ and electron density of $\sim 5000 \text{ cm}^{-3}$, both of which are possibly too low for such a highly compact ($\sim 650 \text{ au}$) H II region. On the other hand, if a more rapid and wider angle precession is present compared to that found by analysis of the radio HH lobes, then this may support N as being the site of shock emission from the jet. However, SE lies along the accepted jet outflow axis and is roughly at the same separation from S as N is. This suggests that if a wider angle precession is present, it is only affecting the northern jet. It is interesting to note that Wheelwright et al. (2012) see this lobe asymmetry in their MIR observations too. Unfortunately, 2MASS and GLIMPSE imagery is saturated, with image defects at N's position prohibiting its nature from being established any further.

In Fig. 10, the position angle of the peak emission for each of G310.1420+00.7583A's lobes is plotted as a function of radius and position angle from A1 (i.e. the MYSO), which shows evidence for precession in the jet's axis. These positions were fitted with a precessing jet model with inclination left as a free parameter. For both the 2013 and 2014 data, the best-fitting model's parameters are tabulated in Table 5. In Fig. 11, this model derived for the 2014 data is plotted over GLIMPSE, MIR images. It can be seen that the jet model's path traces both the east, MIR $4.5 \mu\text{m}$ excess (EGO) and general, extended, radio morphology well. Comparison of the 2013 and 2014 best-fitting models shows that the derived quantities largely agree, apart from the precession angles (19° and 6° for the 2013/2014 data, respectively). This discrepancy between the two models is likely due to deconvolution/imaging errors discussed in Sections 4.2 and 5.2. As with G310.0135+00.3892, assuming that

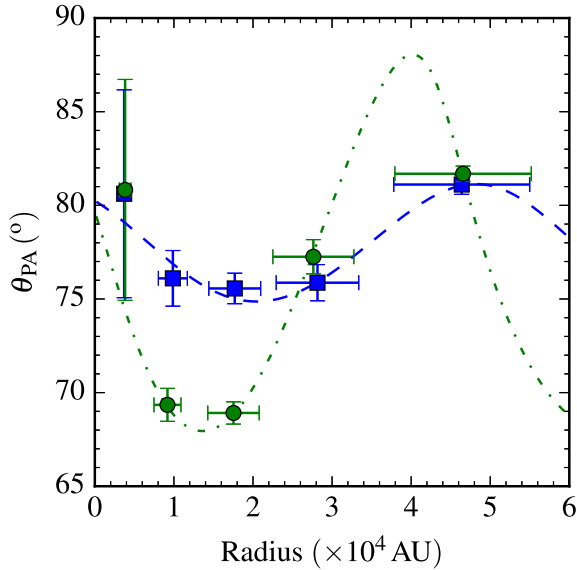


Figure 10. A plot of the radii and position angles of components A2, A3, A4, C, and D relative to A1 during both the 2013 (green circles) and 2014 (blue squares) epochs with their fitted curves (green dot-dashed line and blue dashed line, respectively). For 2013 and 2014 data, θ_{PA} was fixed at 78° , and values for P_{Pr} of 515 and 725 yr, i of 19° and 17° , θ_{Pr} of 19° and 6° and ϕ of -9° and -45° were derived for the 2013 and 2014 models, respectively.

Table 5. A table of the derived parameters from χ^2 fitting of model in parameter space. Errors are calculated by consideration of the distribution of χ^2 in parameter space. Any value with a * next to it was held as a fixed parameter, so that the number of degrees of freedom, $\nu = N_{\text{points}} - N_{\text{op}}$ (N_{op} is the number of open parameters in the fit), is always 1.

Source	Year	θ_{Pr} ($^\circ$)	P_{Pr} (yr)	ϕ ($^\circ$)	i ($^\circ$)	θ_{PA} ($^\circ$)
G310.0135	2014	6^{+1}_{-2}	$15\,480^{+3409}_{-2248}$	308^{+43}_{-26}	42^*	31^*
G310.1420	2013	19^{+2}_{-1}	496^{+27}_{-34}	340^{+15}_{-7}	19^{+3}_{-10}	78^*
	2014	6^{+3}_{-3}	568^{+318}_{-126}	313^{+88}_{-57}	16^{+26}_{-16}	78^*
G313.7654	2014	12^{+2}_{-1}	920^{+82}_{-32}	338^{+11}_{-26}	51^{+3}_{-2}	121^*

the jet precession is due to a binary whose orbital period is the same as the precession period, an orbital radius of 141^{+7}_{-8} or 155^{+58}_{-24} au is inferred, depending on whether the fit parameters for the 2013 or 2014 data are used respectively.

In the case of G313.7654–00.8620, the radii and position angles of A2, B1, B3, C, and D were calculated with respect to the MYSO, A1 (plotted in Fig. 12). Because only the 2014 images detected B3, fitting with inclination as a free parameter was only attempted towards the 2014 lobe positions (in order to have at least one degree of freedom). Component B2 is neglected from this analysis due to its unknown nature and its deviation from the position angles of the other lobes. Fitting yields a precessing jet model with a precession angle of 12^{+20}_{-1} , period of 920^{+82}_{-32} yr, and inclination of 51^{+30}_{-2} , which is shown overlaid upon a GLIMPSE RGB image in Fig. 13. As with the other objects, if a binary companion has induced this precession, a separation for the binary companion of 270^{+19}_{-13} au is inferred. The fitted model does not accurately trace the MIR 4.5 μm excess, in comparison with G310.1420+00.7583A, the diffuse radio emission detected between A2 and C, or the radio lobe G (which is coincident with the H_2 2.122 μm emission lobe, ‘knot 4’ from Caratti o Garatti

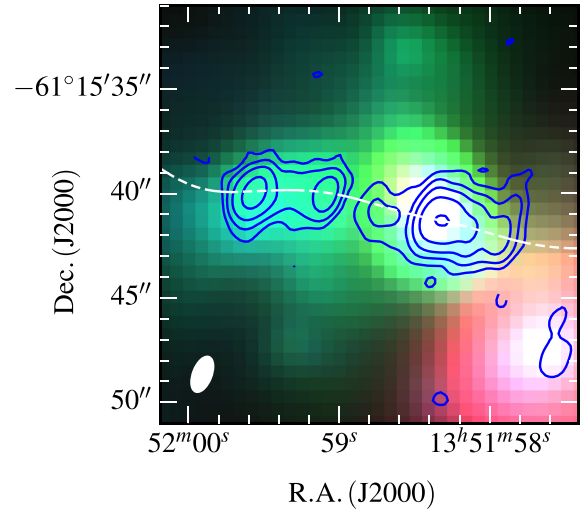


Figure 11. A GLIMPSE RGB image of G310.1420+00.7583A overlaid with contours of the 9 GHz radio flux (contour levels are the same as in panel b of Fig. 4). The jet model uses the fitted values for the 2014 data (see Fig. 10).

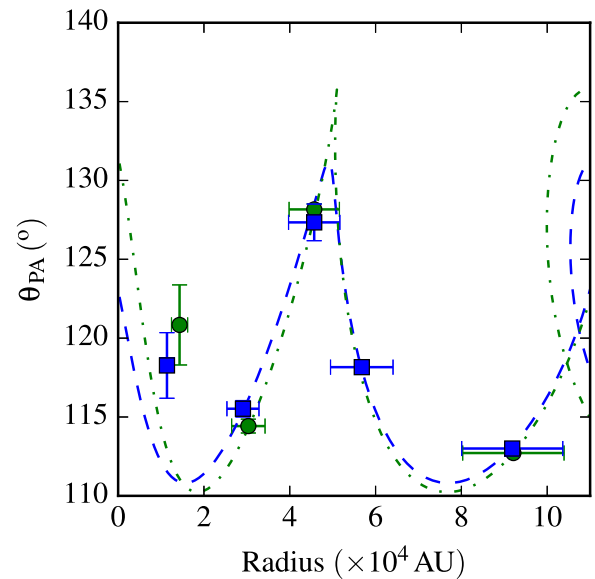


Figure 12. A plot of the radii and position angles for components A2, B1, B3, C, and D of G313.7654–00.8620 (relative to A1) where symbols and fitted lines have the same meaning as in Fig. 11. For 2013 and 2014 data, values for θ_{PA} of 123° and 121° , P_{Pr} of 950 and 995 yr, i of 54° (for both), θ_{Pr} of 15° and 12° and ϕ of 35° and 10° were used for the 2013 and 2014 models, respectively.

et al. 2015). It is possible that G313.7654–00.8620 is a more complex system, and (in addition to periodic precession) a large overall shift in the precession axis may have occurred, on account of G’s position and the results of Caratti o Garatti et al. (2015), from $\sim 98^\circ$ to 121° over a period of approximately 4100 yr, or $5.6 \times 10^{-3} \text{ yr}^{-1}$.

In Fig. 14, the four, inferred precession angles for the sample, and the relevant orbital radii, are plotted. Fitted power laws for precession angle against both period and inferred orbital radius are explicitly stated in equations (2) and (3), respectively, below:

$$\log_{10}(\theta_{Pr}) = (2.20 \pm 0.13) - (0.36 \pm 0.05) \log_{10}(P_{Pr}) \quad (2)$$

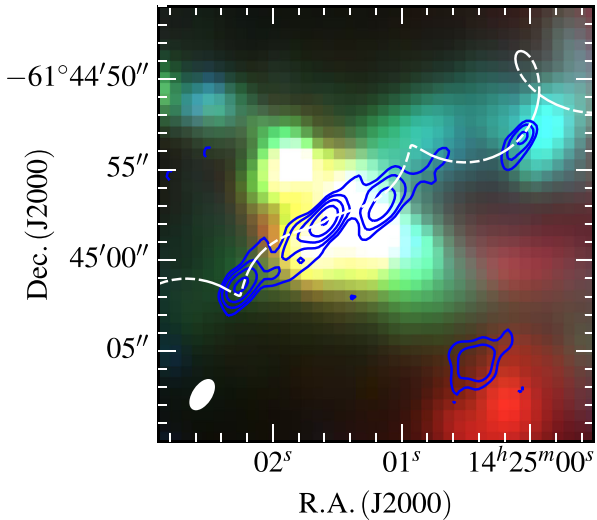


Figure 13. A GLIMPSE RGB image of G313.7654–00.8620 overlaid with contours of the 9 GHz radio flux (contour levels of -4 , 4 , 8 , 15 , 28 , and 54σ , where $\sigma = 9.0 \mu\text{Jy beam}^{-1}$). The jet model uses the fitted values for the 2014 data (see Fig. 12).

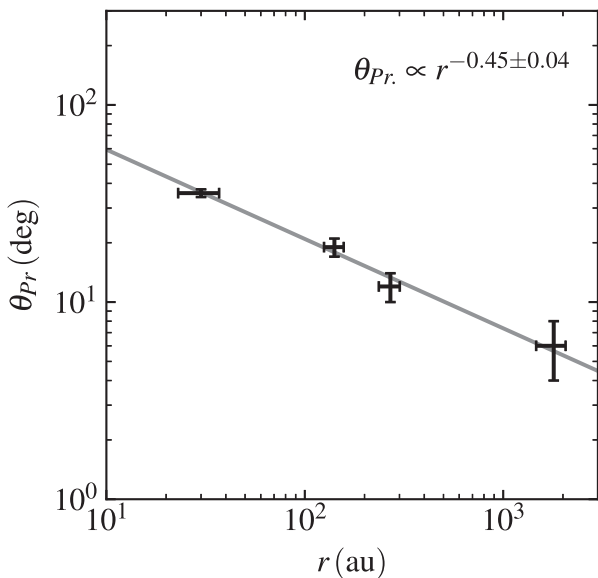


Figure 14. A plot of the precession angle (θ_{Pr}) against inferred orbital radii (r). Orthogonal distance regression (taking into account errors in both variables) was used to fit the power law that is plotted in grey and explicitly stated in equation (3).

$$\log_{10}(\theta_{Pr}) = (2.23 \pm 0.08) - (0.45 \pm 0.04) \log_{10}(r). \quad (3)$$

These relations show that for shorter precession periods/smaller orbital radii for the hypothesized binary companions, a larger precession angle is observed. This agrees with the idea that a closer companion would deflect a jet’s stream to a greater degree, either through gravitational influence upon the ballistic trajectory of jet material or alteration of the disc’s magnetic field. However, to establish this explanation would require both a larger sample than that presented here and direct confirmation of the existence of binary companions.

6 SUMMARY AND CONCLUSIONS

Sensitive radio observations at 6 and 9 GHz were conducted towards a sample of four MYSOs known to harbour ionized jets associated with shock-ionized lobes. This sample was selected from the previous work of Paper I in order to investigate their temporal evolution, faint emission, and precession of their outflow axes. From careful consideration of the observational differences between each epoch’s data set, their subsequent comparison as well as modelling of the relative lobe positions from their sourcing jets, the following can be concluded.

(i) Fainter emission is detected towards three of four jets, which is sourced directly from the thermal jet itself in one object (G263.7434+00.1161), radio Herbig–Harro objects in G310.0135+00.3892, and extra non-thermal emission in G313.7654–00.8620. This suggests that mass-loss in MYSO jets is always occurring, though at highly variable rates.

(ii) Proper motion is detected at the $>3\sigma$ level towards one lobe (C) of G310.1420+00.7583A, with a derived velocity of $1806 \pm 596 \text{ km s}^{-1}$ parallel to the jet’s propagation axis.

(iii) Change in the flux morphology is seen towards a non-thermal lobe (D) of G310.1420+00.7583A, supporting the hypothesis that the emission is the result of an evolving shock, rather than direct emission from the jet’s stream.

(iv) Evidence for precession is found in all objects within the sample, with inferred precession angles ranging from $6^\circ \pm 3^\circ$ to $36^\circ \pm 2^\circ$ and periods from 66 ± 20 to 15480_{-2248}^{+3409} yr. If the assumed precession of jet outflow axes is caused by the bound orbits of binary companions, estimated orbital radii of 30 ± 6 , 1797_{-191}^{+275} , 141_{-8}^{+7} , and 270_{-13}^{+19} au are found for G263.7434+00.1161, G310.0135+00.3892, G310.1420+00.7583A, and G313.7654–00.8620, respectively.

Considering the apparent precessions of the MYSOs observed, it is clear that these four ionized jets are not restricted to a single outflow angle over time. Compared to precession seen towards low-mass examples, it is both more extreme and also more rapid. Definitive variability or proper motions were not observed over a 2 yr period towards the shock-ionized lobes or thermal jets; however, future studies, with longer time baselines, towards a larger sample of objects from Paper I will inform more reliably on these matters. The results presented here therefore form the foundation for such studies and hint that it will produce interesting results in the future.

ACKNOWLEDGEMENTS

SJDP gratefully acknowledges the studentship funded by the Science and Technology Facilities Council of the United Kingdom (STFC). This paper has made use of information from the RMS survey data base (Lumsden et al. 2013) at <http://rms.leeds.ac.uk/>, which was constructed with support from the Science and Technology Facilities Council of the United Kingdom.

REFERENCES

- Anglada G., 1996, in Taylor A. R., Paredes J. M., eds, ASP Conf. Ser. Vol. 93, Radio Emission from the Stars and the Sun. Astron. Soc. Pac., San Francisco, p. 3
- Beuther H., Schilke P., Sridharan T. K., Menten K. M., Walmsley C. M., Wyrowski F., 2002, *A&A*, 383, 892
- Boley P. A. et al., 2016, *A&A*, 586, A78
- Caratti o Garatti A., Stecklum B., Linz H., Garcia Lopez R., Sanna A., 2015, *A&A*, 573, A82
- Caratti o Garatti A. et al., 2016, *A&A*, 589, L4

- Caratti O Garatti A. et al., 2017, Nat. Phys., 13, 276
- Caswell J. L., 1998, MNRAS, 297, 215
- Contreras Y. et al., 2013, A&A, 549, A45
- Curiel S. et al., 2006, ApJ, 638, 878
- Cyganowski C. J. et al., 2008, ApJ, 136, 2391
- Davies B., Hoare M. G., Lumsden S. L., Hosokawa T., Oudmaijer R. D., Urquhart J. S., Mottram J. C., Stead J., 2011, MNRAS, 416, 972
- de Luca M., Giannini T., Lorenzetti D., Massi F., Elia D., Nisini B., 2007, A&A, 474, 863
- Duchêne G., Kraus A., 2013, ARA&A, 51, 269
- Elias J. H., 1980, ApJ, 241, 728
- Frank A. et al., 2014, Protostars and Planets VI. Univ. Arizona Press, Tucson, p. 451
- Green J. A. et al., 2012, MNRAS, 420, 3108
- Gullbring E., Hartmann L., Briceño C., Calvet N., 1998, ApJ, 492, 323
- Guzmán A. E., Garay G., Brooks K. J., 2010, ApJ, 725, 734
- Ilee J. D. et al., 2013, MNRAS, 429, 2960
- Kraus S. et al., 2010, Nature, 466, 339
- Liseau R., Lorenzetti D., Nisini B., Spinoglio L., Moneti A., 1992, A&A, 265, 577
- Lumsden S. L., Hoare M. G., Urquhart J. S., Oudmaijer R. D., Davies B., Mottram J. C., Cooper H. D. B., Moore T. J. T., 2013, ApJS, 208, 11
- Marti J., Rodríguez L. F., Reipurth B., 1993, ApJ, 416, 208
- Marti J., Rodríguez L. F., Reipurth B., 1995, ApJ, 449, 184
- Martí J., Rodríguez L. F., Reipurth B., 1998, ApJ, 502, 337
- Massi F., de Luca M., Elia D., Giannini T., Lorenzetti D., Nisini B., 2007, A&A, 466, 1013
- Meyer D. M.-A., Vorobyov E. I., Kuiper R., Kley W., 2017, MNRAS, 464, L90
- Moraghan A., Lee C.-F., Huang P.-S., Vaidya B., 2016, MNRAS, 460, 1829
- Mottram J. C. et al., 2011, ApJ, 730, L33
- Purser S. J. D. et al., 2016, MNRAS, 460, 1039 (Paper I)
- Reynolds S. P., 1986, ApJ, 304, 713
- Rodríguez L. F., Garay G., Brooks K. J., Mardones D., 2005, ApJ, 626, 953
- Rodríguez L. F., Moran J. M., Franco-Hernández R., Garay G., Brooks K. J., Mardones D., 2008, ApJ, 135, 2370
- Sault R. J., Teuben P. J., Wright M. C. H., 1995, in Shaw R. A., Payne H. E., Hayes J. J. E., eds, ASP Conf. Ser. Vol. 77, Astronomical Data Analysis Software and Systems IV. Astron. Soc. Pac., San Francisco, p. 433
- Scaife A. M. M. et al., 2011, MNRAS, 415, 893
- Sheikhnezami S., Fendt C., 2015, ApJ, 814, 113
- Shu F. H., Adams F. C., Lizano S., 1987, ARA&A, 25, 23
- Urquhart J. S., Busfield A. L., Hoare M. G., Lumsden S. L., Clarke A. J., Moore T. J. T., Mottram J. C., Oudmaijer R. D., 2007, A&A, 461, 11
- Urquhart J. S. et al., 2009, A&A, 507, 795
- Walsh A. J., Burton M. G., Hyland A. R., Robinson G., 1998, MNRAS, 301, 640
- Wheelwright H. E., de Wit W. J., Oudmaijer R. D., Hoare M. G., Lumsden S. L., Fujiyoshi T., Close J. L., 2012, A&A, 540, A89
- Wolfire M. G., Konigl A., 1991, ApJ, 383, 205

APPENDIX A: SUPPLEMENTARY TABLES

Table A1. A table of lobe positions, integrated fluxes, and deconvolved dimensions at 9 GHz for the 2013 epoch. The final column indicates which robustness was employed in the clean map.

Source	Lobe	α (J2000)	$\delta\alpha$ (arcsec)	δ (J2000)	$\delta\delta$ (arcsec)	S_9 (μ Jy)	θ_{Maj} (arcsec)	θ_{Min} (arcsec)	θ_{PA} ($^\circ$)	R
G263.7434+00.1611	N	08 ^h 48 ^m 48 ^s .47	0.019	−43°32′24″.0	0.064	615 ± 79	1.32 ± 0.31	0.55 ± 0.14	175.0 ± 13.0	0.5
	S2	—	—	—	—	<80 ± 27	—	—	—	0.5
	S	08 ^h 48 ^m 48 ^s .66	0.014	−43°32′28″.7	0.068	1026 ± 110	2.34 ± 0.22	0.59 ± 0.12	6.1 ± 3.2	0.5
G310.0135+00.3892	SE	08 ^h 48 ^m 48 ^s .87	0.206	−43°32′32″.9	0.596	206 ± 87	3.41 ± 1.91	1.03 ± 0.94	163.0 ± 41.0	2
	N	13 ^h 51 ^m 37 ^s .85	0.013	−61°39′06″.3	0.012	709 ± 85	<0.35	<0.22	—	−1
	S	13 ^h 51 ^m 37 ^s .85	0.032	−61°39′07″.8	0.022	413 ± 76	0.41 ± 0.16	0.16 ± 0.15	79.0 ± 83.0	−1
G310.1420+00.7583A	SW	13 ^h 51 ^m 37 ^s .73	0.055	−61°39′09″.1	0.119	149 ± 65	—	—	—	−1
	A1	13 ^h 51 ^m 58 ^s .37	0.008	−61°15′41″.2	0.007	1848 ± 152	0.55 ± 0.04	0.45 ± 0.04	92.0 ± 21.0	−1
	A2	13 ^h 51 ^m 58 ^s .26	0.006	−61°15′41″.5	0.008	909 ± 83	—	—	—	−1
	A3	13 ^h 51 ^m 58 ^s .16	0.021	−61°15′41″.8	0.015	1938 ± 182	1.27 ± 0.06	0.46 ± 0.05	58.4 ± 2.1	−1
	A4	13 ^h 51 ^m 57 ^s .94	0.018	−61°15′42″.3	0.035	660 ± 97	0.85 ± 0.12	0.28 ± 0.17	1.9 ± 7.0	−1
	B	13 ^h 51 ^m 58 ^s .71	0.068	−61°15′40″.7	0.052	311 ± 66	—	—	—	0.5
	C	13 ^h 51 ^m 59 ^s .10	0.044	−61°15′40″.0	0.024	1306 ± 139	2.00 ± 0.13	0.53 ± 0.17	78.3 ± 3.0	0.5
G313.7654−00.8620	D	13 ^h 51 ^m 59 ^s .55	0.018	−61°15′40″.0	0.017	2139 ± 178	1.44 ± 0.07	1.00 ± 0.09	97.0 ± 12.0	0.5
	A1	14 ^h 25 ^m 01 ^s .59	0.013	−61°44′57″.8	0.018	603 ± 58	0.43 ± 0.23	0.25 ± 0.14	47.0 ± 64.0	0.5
	A2	14 ^h 25 ^m 01 ^s .81	0.065	−61°44′58″.8	0.150	165 ± 46	1.48 ± 0.53	0.24 ± 0.50	164.0 ± 26.0	0.5
	B1	14 ^h 25 ^m 01 ^s .10	0.086	−61°44′55″.9	0.085	299 ± 62	1.58 ± 0.36	0.85 ± 0.48	125.0 ± 23.0	0.5
	B2	14 ^h 25 ^m 01 ^s .21	0.059	−61°44′57″.9	0.082	145 ± 36	0.58 ± 0.48	0.36 ± 0.26	40.0 ± 47.0	0.5
	B3	14 ^h 25 ^m 00 ^s .72	0.122	−61°44′55″.1	0.192	88 ± 38	0.96 ± 0.74	0.55 ± 0.36	18.0 ± 35.0	0.5
	C	14 ^h 25 ^m 02 ^s .25	0.031	−61°45′01″.3	0.038	444 ± 58	0.85 ± 0.22	0.82 ± 0.28	72.0 ± 86.0	0.5
	D	14 ^h 25 ^m 00 ^s .07	0.043	−61°44′53″.3	0.057	160 ± 33	<0.72	<0.29	—	0.5

Table A2. A table of lobe positions, integrated fluxes, and deconvolved dimensions at 6 GHz for the 2014 epoch. The final column indicates which robustness was employed in the clean map. Those components with a ¹ above their name are extended and therefore their peak flux positions are given, whose errors cover half of their 3 σ spatial extent. Their provided fluxes are integrated over the 3 σ contours.

Source	Lobe	α (J2000)	$\delta\alpha$ (arcsec)	δ (J2000)	$\delta\delta$ (arcsec)	S_6 (μ Jy)	θ_{Maj} (arcsec)	θ_{Min} (arcsec)	θ_{PA} ($^\circ$)	R
G263.7434+00.1161	N	08 ^h 48 ^m 48 ^s .48	0.005	−43°32′23″.9	0.027	626 ± 43	1.40 ± 0.19	0.50 ± 0.03	177.1 ± 3.6	0.5
	S2	08 ^h 48 ^m 48 ^s .63	0.009	−43°32′57″.7	0.050	319 ± 28	1.13 ± 0.49	0.35 ± 0.17	168.0 ± 21.0	0.5
	S	08 ^h 48 ^m 48 ^s .65	0.004	−43°32′28″.5	0.029	767 ± 52	2.24 ± 0.13	0.62 ± 0.05	5.9 ± 2.0	0.5
	SE	08 ^h 48 ^m 48 ^s .83	0.035	−43°32′33″.4	0.365	126 ± 22	5.18 ± 1.09	0.64 ± 0.23	178.7 ± 2.7	0.5
G310.0135+00.3892	N	13 ^h 51 ^m 37 ^s .87	0.005	−61°39′06″.2	0.009	707 ± 53	0.28 ± 0.07	0.15 ± 0.12	87.0 ± 75.0	−1
	S	13 ^h 51 ^m 37 ^s .87	0.013	−61°39′07″.7	0.022	347 ± 37	0.50 ± 0.16	0.35 ± 0.20	155.0 ± 89.0	−1
	SW	13 ^h 51 ^m 37 ^s .73	0.135	−61°39′09″.3	0.168	126 ± 35	<2.60	<0.51	–	−1
	HH0 ¹	13 ^h 51 ^m 41 ^s .84	2.4	−61°38′18″.7	3.3	145 ± 19	–	–	–	0.5
	HH1 ¹	13 ^h 51 ^m 48 ^s .13	2.7	−61°36′46″.2	3.2	422 ± 48	–	–	–	0.5
	HH2 ¹	13 ^h 51 ^m 55 ^s .35	1.6	−61°35′38″.6	1.8	121 ± 21	–	–	–	0.5
G310.1420+00.7583A	A1+A2	13 ^h 51 ^m 58 ^s .33	0.004	−61°15′41″.2	0.006	2744 ± 177	0.84 ± 0.03	0.55 ± 0.05	62.6 ± 5.4	−1
	A3	13 ^h 51 ^m 58 ^s .18	0.006	−61°15′41″.7	0.010	2053 ± 144	1.09 ± 0.04	0.42 ± 0.06	37.5 ± 3.1	−1
	A4	13 ^h 51 ^m 57 ^s .96	0.011	−61°15′42″.0	0.021	888 ± 83	0.93 ± 0.10	0.43 ± 0.15	37.8 ± 9.6	−1
	B	13 ^h 51 ^m 58 ^s .70	0.027	−61°15′41″.0	0.102	369 ± 51	2.24 ± 0.36	0.71 ± 0.21	175.8 ± 6.6	0.5
	C	13 ^h 51 ^m 59 ^s .12	0.018	−61°15′40″.0	0.020	1508 ± 115	1.91 ± 0.09	1.09 ± 0.18	80.7 ± 5.8	0.5
G313.7654−00.8620	D	13 ^h 51 ^m 59 ^s .55	0.006	−61°15′40″.1	0.011	2474 ± 157	1.31 ± 0.05	1.15 ± 0.07	136.0 ± 16.0	0.5
	A1	14 ^h 25 ^m 01 ^s .59	0.012	−61°44′57″.9	0.024	338 ± 30	–	–	–	0.5
	A2	14 ^h 25 ^m 01 ^s .69	0.076	−61°44′58″.2	0.064	426 ± 47	3.42 ± 0.28	0.70 ± 0.28	122.6 ± 3.1	0.5
	B1	14 ^h 25 ^m 01 ^s .10	0.044	−61°44′56″.0	0.043	231 ± 28	–	–	–	0.5
	B2	14 ^h 25 ^m 01 ^s .18	0.049	−61°44′57″.5	0.047	213 ± 27	–	–	–	0.5
	B3	14 ^h 25 ^m 00 ^s .71	0.160	−61°44′54″.6	0.176	118 ± 30	2.15 ± 0.90	1.20 ± 0.77	122.0 ± 51.0	0.5
	D	14 ^h 25 ^m 00 ^s .09	0.043	−61°44′53″.3	0.060	165 ± 24	<1.20	<0.84	–	0.5
	F	14 ^h 25 ^m 04 ^s .70	0.064	−61°44′50″.3	0.185	85 ± 22	<2.2	<0.77	–	0.5
G	14 ^h 24 ^m 57 ^s .07	0.581	−61°44′53″.2	0.236	171 ± 59	4.75 ± 1.56	1.09 ± 0.88	101 ± 15	0.5	

Table A3. A table of lobe positions, integrated fluxes, and deconvolved dimensions at 9 GHz for the 2014 epoch. The final column indicates which robustness was employed in the clean map.

Source	Lobe	α (J2000)	$\delta\alpha$ (arcsec)	δ (J2000)	$\delta\delta$ (arcsec)	S_9 (μ Jy)	θ_{Maj} (arcsec)	θ_{Min} (arcsec)	θ_{PA} ($^\circ$)	R
G263.7434+00.1161	N	08 ^h 48 ^m 48 ^s .48	0.004	−43°32′23″.8	0.026	594 ± 44	1.40 ± 0.14	0.39 ± 0.03	176.1 ± 2.0	0.5
	Radio Star	08 ^h 48 ^m 48 ^s .63	0.007	−43°32′57″.7	0.037	363 ± 31	1.04 ± 0.27	0.27 ± 0.07	167.8 ± 7.8	0.5
	S	08 ^h 48 ^m 48 ^s .66	0.003	−43°32′28″.5	0.023	837 ± 58	1.85 ± 0.10	0.43 ± 0.04	5.8 ± 1.6	0.5
	SE	08 ^h 48 ^m 48 ^s .82	0.047	−43°32′33″.1	0.468	135 ± 29	5.29 ± 1.27	0.73 ± 0.18	177.2 ± 2.4	0.5
G310.0135+00.3892	N	13 ^h 51 ^m 37 ^s .86	0.005	−61°39′06″.2	0.013	695 ± 66	<0.46	<0.06	–	−1
	S	13 ^h 51 ^m 37 ^s .87	0.006	−61°39′07″.6	0.018	481 ± 53	–	–	–	−1
	SW	13 ^h 51 ^m 37 ^s .75	0.045	−61°39′08″.9	0.078	93 ± 32	–	–	–	−1
G310.1420+00.7583A	A1	13 ^h 51 ^m 58 ^s .39	0.006	−61°15′41″.2	0.014	1462 ± 125	0.66 ± 0.07	0.28 ± 0.03	162.4 ± 4.3	−1
	A2	13 ^h 51 ^m 58 ^s .28	0.006	−61°15′41″.4	0.012	1842 ± 149	0.61 ± 0.07	0.41 ± 0.03	171.0 ± 12.0	−1
	A3	13 ^h 51 ^m 58 ^s .14	0.024	−61°15′41″.7	0.045	1295 ± 160	1.36 ± 0.14	0.81 ± 0.07	163.4 ± 8.0	−1
	A4	13 ^h 51 ^m 57 ^s .93	0.018	−61°15′41″.9	0.058	570 ± 94	1.00 ± 0.22	0.32 ± 0.15	7.1 ± 13.9	−1
	B	13 ^h 51 ^m 58 ^s .72	0.055	−61°15′41″.0	0.100	357 ± 69	1.40 ± 0.39	0.75 ± 0.64	35.0 ± 36.0	0.5
	C	13 ^h 51 ^m 59 ^s .13	0.037	−61°15′40″.0	0.031	1154 ± 120	1.82 ± 0.15	0.82 ± 0.33	88.6 ± 8.8	0.5
	D	13 ^h 51 ^m 59 ^s .56	0.001	−61°15′40″.0	0.013	2079 ± 151	1.13 ± 0.06	0.74 ± 0.11	95.8 ± 8.0	0.5
	G313.7654−00.8620	A1	14 ^h 25 ^m 01 ^s .59	0.012	−61°44′57″.9	0.015	451 ± 39	–	–	–
A2		14 ^h 25 ^m 01 ^s .74	0.165	−61°44′58″.4	0.150	469 ± 67	4.90 ± 0.56	1.09 ± 0.15	130.6 ± 2.1	0.5
B1		14 ^h 25 ^m 01 ^s .10	0.061	−61°44′56″.2	0.071	277 ± 42	1.62 ± 0.34	0.99 ± 0.21	132.0 ± 25.0	0.5
B2		14 ^h 25 ^m 01 ^s .18	0.068	−61°44′57″.5	0.081	146 ± 26	<1.70	<0.29	–	0.5
B3		14 ^h 25 ^m 00 ^s .72	0.195	−61°44′54″.8	0.218	81 ± 27	1.97 ± 1.11	0.32 ± 0.34	134.0 ± 33.0	0.5
C		14 ^h 25 ^m 02 ^s .25	0.023	−61°45′01″.4	0.028	372 ± 38	0.87 ± 0.21	0.35 ± 0.11	125.0 ± 19.0	0.5
D		14 ^h 25 ^m 00 ^s .08	0.038	−61°44′53″.4	0.056	164 ± 24	–	–	–	0.5
F		14 ^h 25 ^m 04 ^s .68	0.104	−61°44′50″.1	0.105	85 ± 25	–	–	–	0.5
G	14 ^h 24 ^m 57 ^s .04	0.130	−61°44′54″.1	0.125	51 ± 18	–	–	–	0.5	

APPENDIX B: SUPPLEMENTARY FIGURES

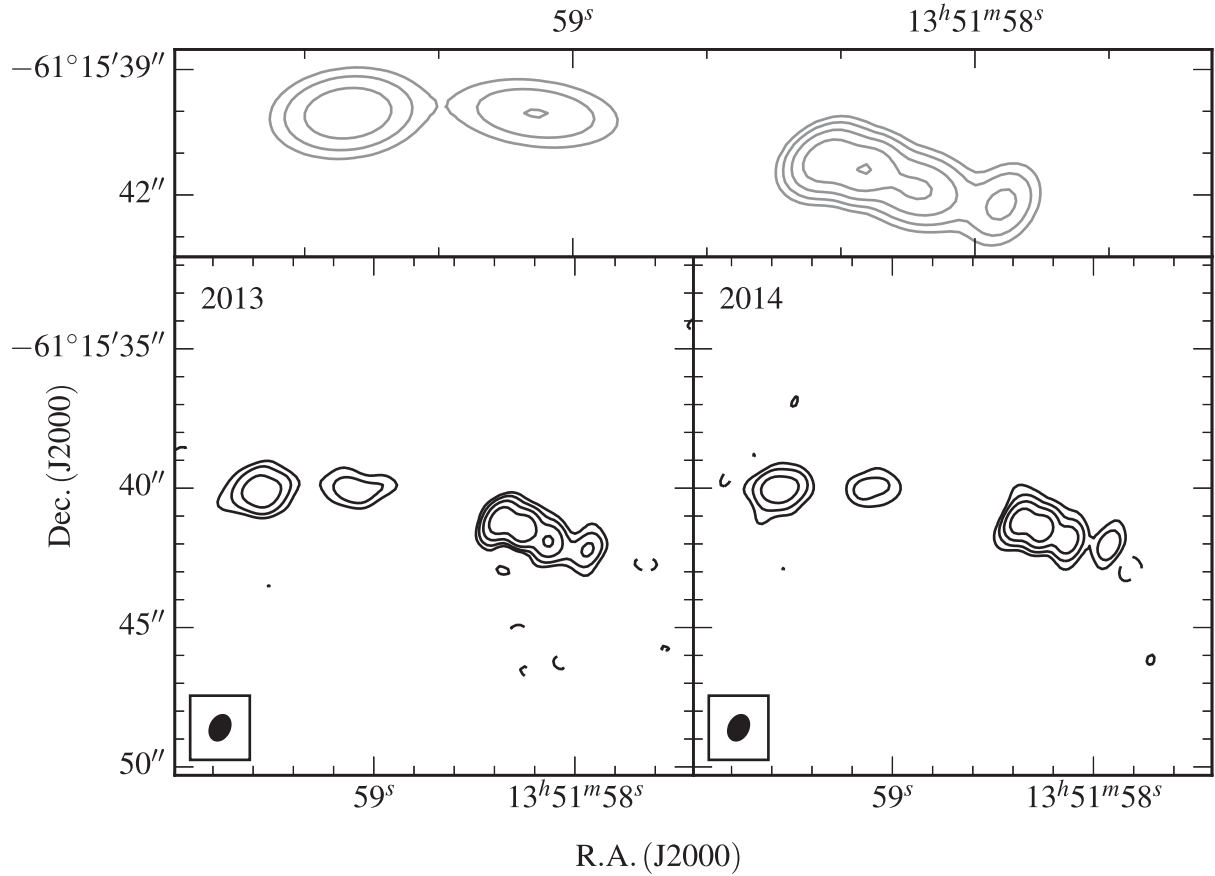


Figure B1. Clean maps of the synthetic data at 9 GHz (bottom-left and -right plots). The top plot represents the model used to generate the synthetic visibilities convolved with the common beam used in both synthetic clean maps ($0.94 \text{ arcsec} \times 0.68 \text{ arcsec}$, $\theta_{\text{PA}} = -26^{\circ}.3$, shown in the bottom left of each clean map). All contours are logarithmically spaced from 3σ (where $\sigma = 23.0 \mu\text{Jy beam}^{-1}$, the noise in the 2013 synthetic clean map) to 95 per cent the maximum flux in the model's image, specifically $-3, 3, 6, 14, 29,$ and 63σ .

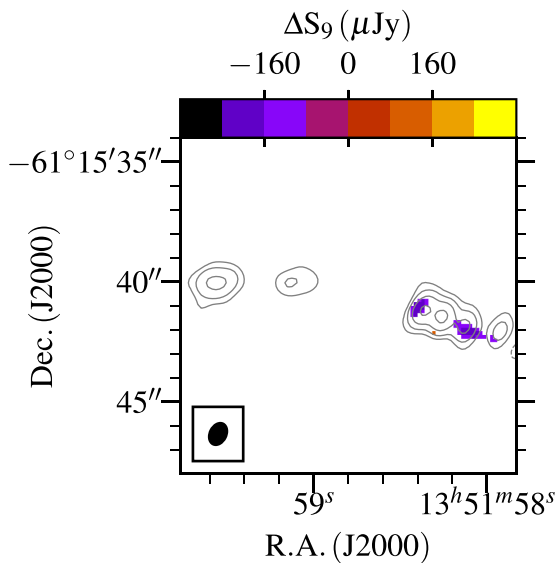


Figure B2. A map of pixel-to-pixel flux differences between 2013 and 2014 synthetic clean maps (colour scale). The grey contours are the same as per Fig. 9.

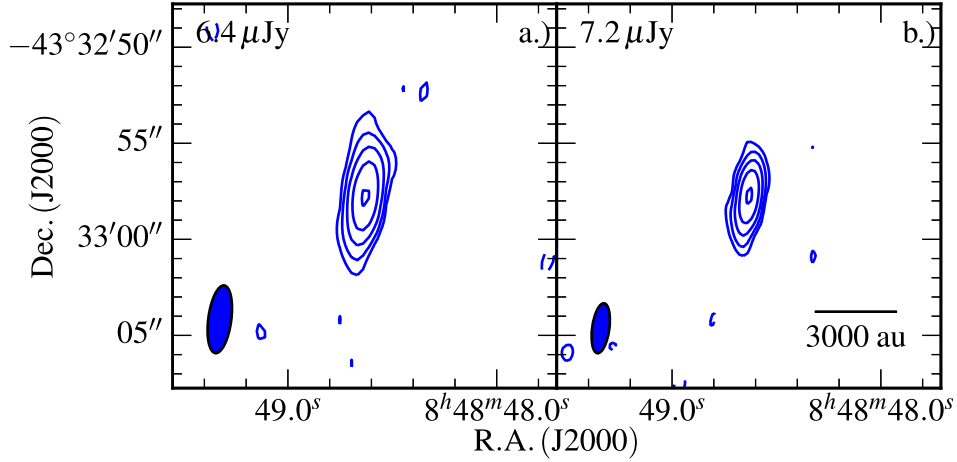


Figure B3. Primary beam-corrected, radio contour maps of lobe S2 detected in the primary beam of our observation of G263.7434+00.1161 utilizing a robustness of 0.5 at (a) 6 GHz; (b) 9 GHz. Restoring beams used are illustrated in the bottom-left corners (same dimensions as in Fig. 1) and contours are $(-3, 3, 6, 11, 22, 44) \times \sigma$ and $(-3, 3, 6, 11, 22, 42) \times \sigma$ for the 6 and 9 GHz data, respectively, where σ is the noise in the image indicated in the top-left corner of each sub-plot.

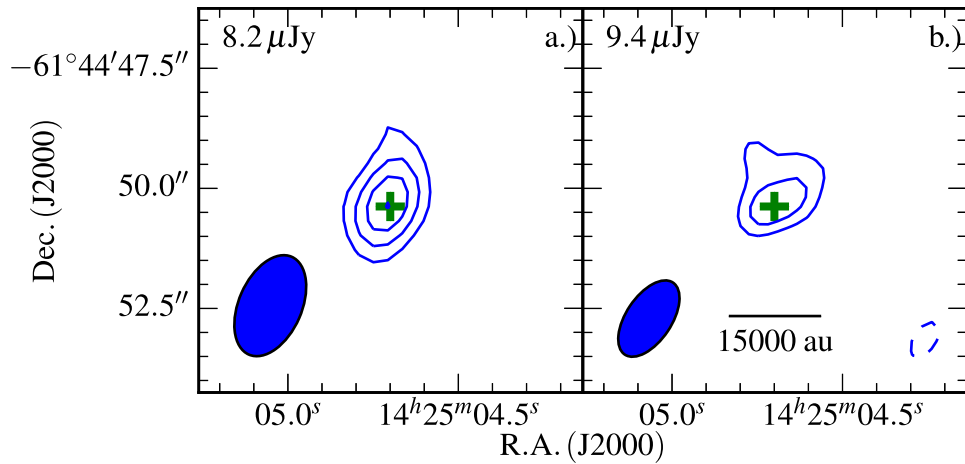


Figure B4. Primary beam-corrected, radio contour maps of 'F' towards G313.7654-00.8620 utilizing a robustness of 0.5 at (a) 6 GHz; (b) 9 GHz. Restoring beams used are illustrated in the bottom-left corners (same dimensions as in Fig. 5) and contours are $(-3, 3, 5, 7) \times \sigma$, where σ is the noise in the image indicated in the top-left corner of each sub-plot. The green cross indicates a CH₃OH maser detected in the 6 GHz band whose positional uncertainties are <0.1 arcsec.

APPENDIX C: PRECESSION MODEL

A basic illustration of the model used for a precessing jet is presented in Fig. C1, which uses the following assumptions:

- (i) ballistic trajectories are adhered to;
- (ii) biaxial symmetry of the jet at the point of collimation and ejection;
- (iii) velocity assumed to be constant along the length of the jet;
- (iv) precession occurs at a constant angle and period;

$$r(t) = vt \sin\left(\frac{\theta_{Pr}}{2}\right) \quad (C1)$$

$$x(t) = r(t) \cos\left(\frac{2\pi t}{P_{Pr}}\right) \quad (C2)$$

$$y(t) = r(t) \sin\left(\frac{2\pi t}{P_{Pr}}\right) \quad (C3)$$

$$z(t) = vt \cos\left(\frac{\theta_{Pr}}{2}\right). \quad (C4)$$

Once the (x, y, z) coordinates of the jet are established for a position angle of 0° and inclination of 0° , a rotation is then applied around the x -, y -, and z -axes for position angle, inclination, and present jet angle (θ_{PA} , i , and ϕ), respectively. For any point on the jet, $p(x, y, z)$, the final rotated coordinate, p_{rot} , is calculated according to equation (C8):

$$R_x(\theta_{PA}) = \begin{bmatrix} 1 & 0 & 0 \\ 0 & \cos(\theta_{PA}) & -\sin(\theta_{PA}) \\ 0 & \sin(\theta_{PA}) & \cos(\theta_{PA}) \end{bmatrix} \quad (C5)$$

$$R_y(i) = \begin{bmatrix} \cos(i) & 0 & \sin(i) \\ 0 & 1 & 0 \\ -\sin(i) & 0 & \cos(i) \end{bmatrix} \quad (C6)$$

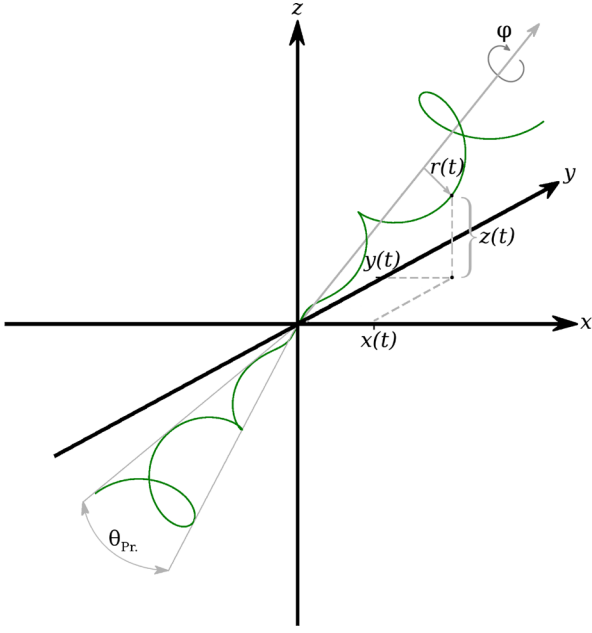


Figure C1. An illustration showing the basic setup of the jet model used to fit radio-lobe positional data in the main text. Symbols in the diagram are as follows: i is the inclination angle, θ_{PA} is the position angle in the sky, θ_{Pr} is the precession angle, and $x(t)$, $y(t)$, and $z(t)$ are the (x, y, z) coordinates of a point in the jet's stream (green curve) at a time, t .

$$R_z(\phi) = \begin{bmatrix} \cos(\phi) & -\sin(\phi) & 0 \\ \sin(\phi) & \cos(\phi) & 0 \\ 0 & 0 & 1 \end{bmatrix} \quad (C7)$$

$$p_{rot} = R_y(\theta_{PA}) \cdot (R_x(i) \cdot (R_z(\phi) \cdot p(x, y, z))). \quad (C8)$$

Axes are defined so that the x -axis points towards the observer and, therefore, the y - and z -axes represent right ascension and declination, respectively. This allows us to compare the observables r and θ (radial distance and position angle from the jet origin, respectively) with the model, since the (y, z) coordinate of any point in the rotated model is equivalent to (α, δ) offsets from the jet's origin. Due to the assumption of biaxial symmetry, it is possible to rotate any lobe coordinate through π rad in position angle.

For fitting observational data, a number of models are produced using a range of values for i , θ_{Pr} , ϕ , P_{Pr} , and θ_{PA} . For each model, the reduced χ^2 value is calculated according to the following equation:

$$\chi_v^2 = \frac{1}{\nu} \sum_{i=0}^n \frac{(|x_i - \mu_i| - Y)^2}{\sigma_i^2}, \quad (C9)$$

where x_i , μ_i , σ_i , ν , and Y are the measured value, model value, measurement error, degrees of freedom, and Yates' correction factor ($Y = 0.5$ if $\nu = 1$, otherwise $Y = 0$), respectively. Over all tested models, the one which minimizes χ_v^2 is chosen. From jets with multiple lobes, it is possible to place a lower limit on θ_{Pr} , approximate θ_{PA} , and in some circumstances place an upper limit on P_{Pr} (should the lobes appear to move through $> \frac{3\pi}{2}$ rad) from inspection of the (r, θ) lobe coordinates. This allows us to constrain the extent of parameter space covered during our fitting process.

A shortcoming of this approach is that any number of models can be fitted through any number of points by reducing P_{Pr} to shorter times. Therefore, we choose the simplest model with the longest precession period as the 'correct' one.

This paper has been typeset from a $\text{\TeX}/\text{\LaTeX}$ file prepared by the author.